

An X-ray spectral study of 24 type-1 active galactic nuclei

C. S. Reynolds[★]

Institute of Astronomy, Madingley Road, Cambridge CB3 0HA

ABSTRACT

I present a study of the X-ray spectral properties of a sample containing 24 type-1 active galactic nuclei using the medium spectral resolution of *ASCA*. The sample consists of 20 radio-quiet objects (18 Seyfert 1 galaxies and 2 radio-quiet quasars) and 4 radio-loud objects (3 broad-line radio galaxies and 1 radio-loud quasar). A simple power-law continuum absorbed by Galactic material provides a very poor description of the spectra of most objects. Deviations from the power-law form are interpreted in terms of X-ray reprocessing/absorption processes. In particular, at least half of the objects show K-shell absorption edges of warm oxygen (O VII and O VIII) characteristic of optically-thin, photoionized material along the line-of-sight to the central engine, the so-called warm absorber. The amount and presence of this absorption is found to depend on either the luminosity or radio-properties of the objects: luminous and/or radio-loud objects are found to possess less ionized absorption. This ambiguity exists because the radio-loud objects are also amongst the most luminous of the sample. It is also found that objects with significant optical reddening display deep O VII edges. The converse is true with two possible exceptions (NGC 3783 and NGC 3516). Coupled with other evidence resulting from detailed study of particular objects, this suggests the existence of dusty warm plasma. A radiatively driven outflow originating from the molecular torus is probably the source of this plasma. Rapid variability of the warm absorber also points to there being another component closer to the central source and probably situated within the broad line region (BLR). Independent evidence for such an optically-thin, highly ionized BLR component comes from detailed optical/UV studies.

Spectral features at energies characteristic of cold iron $K\alpha$ emission are common. Such emission is expected to arise from the fluorescence of cold iron in optically-thick material when illuminated by the primary X-ray continuum. Radio-quiet objects have iron emission well described as originating from either the inner regions of an accretion disk or, in a small number of cases, from the molecular torus. Two of the radio-loud objects (3C 120 and 3C 382) have a much broader feature which presents problems for the relativistic disk model. The presence of radio-jets may be important in forming this spectral feature.

Key words: galaxies: active - X-rays: galaxies - galaxies: Seyfert - plasmas - accretion, accretion disks

1 INTRODUCTION

The high-energy emission of active galactic nuclei (AGN) originate from the innermost regions of an accretion flow onto a putative supermassive black hole. It is widely believed that much of the accretion energy is radiated as X-rays and γ -rays and that reprocessing of this energy by circumnuclear material leads to much of the observed UV, optical and IR luminosity. The X-ray spectrum (~ 0.1 –100 keV) of type-1

AGN (i.e. those displaying broad optical/UV emission lines) can be well approximated by a power-law with photon index $\Gamma \sim 2$. Deviations from a power-law form can usually be interpreted as the effects of X-ray reprocessing. A detailed study of this reprocessing yields direct information on the geometry and state of matter in the central engines of these objects.

The first clear sign of atomic features in the X-ray spectra of AGN came with *EXOSAT* and *Ginga* observations of nearby Seyfert 1 galaxies which found evidence for the fluorescent $K\alpha$ emission line (at 6.4 keV) of cold iron (Nandra et al. 1989; Matsuoka et al. 1990). *Ginga* also discovered

[★] Present address: JILA, University of Colorado, Boulder, CO 80309-0440, USA

a spectral flattening above ~ 10 keV (Nandra, Pounds & Stewart 1990; Nandra & Pounds 1994). These features were explained as due to ‘reflection’ of the primary (power-law) X-ray continuum by cold optically-thick material out of the line-of-sight to the observer (Guilbert & Rees 1988; Lightman & White 1988; George & Fabian 1991; Matt, Perola & Piro 1991). The superior spectral resolution of the solid-state imaging spectrometers (SIS) on board *ASCA* (Tanaka, Inoue & Holt 1994) allowed dramatic advances to be made. Many Seyfert 1 galaxies were found to have broad iron lines (with FWHM ~ 0.1 – $0.2c$; Mushotzky et al. 1995). In particular, a long (4 day) *ASCA* observation of MCG–6–30–15 found the line to be broad and skewed in exactly the sense expected if the reprocessing material were the innermost parts of an accretion disk around a black hole (Tanaka et al. 1995; Fabian et al. 1995; Iwasawa et al. 1996). The characteristic line profile results from the combined effects of Doppler shifts, relativistic aberration and gravitational redshifts. Alternative interpretations for the observed line profile do not seem viable (Fabian et al. 1995). This was the first direct evidence for strong gravitational effects in the vicinity of a putative black hole.

X-ray absorption by partially-ionized, optically-thin material, along the line-of-sight to the central engine, the so-called warm absorber, is another prominent feature in the X-ray spectrum of many AGN. The presence of such gas was first postulated in order to explain the unusual form of the X-ray spectrum of the QSO MR 2251–178 (Halpern 1984; Pan, Stewart & Pounds 1990). Further evidence for such material came from *Ginga* observations of nearby Seyfert 1 galaxies which suggested the presence of K-shell absorption edges of highly ionized iron (Nandra, Pounds & Stewart 1990; Nandra et al. 1991; Nandra & Pounds 1994). However, it is unclear how these conclusions were affected by an over-simplified treatment of the fluorescent iron emission line discussed above. The *ROSAT* position sensitive proportional counter (PSPC) also discovered probable K-shell absorption edges due to O VII and O VIII (Nandra & Pounds 1992; Nandra et al. 1993; Fiore et al. 1993; Turner et al. 1993a). Unfortunately, due to the limited bandpass and spectral resolution of *ROSAT* other explanations for the observed features, such as a complex soft excess or partial covering by a cold absorber, could not be firmly ruled out.

ASCA confirmed the presence of prominent O VII and O VIII edges (at rest energies of 0.74 keV and 0.87 keV respectively) in the X-ray spectra of several bright Seyfert 1 galaxies. The high ionization state strongly suggests it to be photoionized material situated within ~ 10 pc of the primary continuum source. Furthermore, *ASCA* performance verification (PV) observations of MCG–6–30–15 found the warm absorber to be variable on timescales down to several hours (Fabian et al. 1994a; Reynolds et al. 1995). The long *ASCA* observation of this object clarified the nature of the variations: the optical depth of the O VII edge was found to remain constant on timescales of months to years whereas the depth of the O VIII edge was found to anti-correlate with the primary flux on timescales less than $\sim 10^4$ s (Otani et al. 1996). These observations lead to a two-zone warm absorber model for MCG–6–30–15: an inner absorber is responsible for much of the O VIII edge and responds to changes in the ionizing continuum on timescales $\lesssim 10^4$ s whereas the O VII edge largely results from a tenuous outer absorber. The long

recombination timescale in the tenuous outer absorber produces the observed constancy of the absorption edge depth.

Despite these observational advances, the origin of the warm absorbing material and its relation to other known structures within the central engine remains unknown. The variability results for MCG–6–30–15 suggest the inner absorber to be at radii characteristic of the broad line region (BLR; $r \lesssim 10^{17}$ cm) and the outer absorber to be at scales associated with the obscuring torus and Seyfert 2 scattering medium ($r \gtrsim 1$ pc). Both of these structures had been previously considered as possible candidates for producing the warm material (Krolik & Kallman 1987; Netzer 1993; Reynolds & Fabian 1995). However, the general applicability of these results to other AGN is uncertain. An important step would be the analysis of an unbiased sample of AGN with the medium spectral resolution offered by *ASCA* in order to assess the frequency of occurrence of warm absorbers and their relation to other observable properties.

In this paper I present an analysis of the *ASCA* data for a sample of 24 bright type-1 AGN including 18 Seyfert 1 galaxies, 3 broad-line radio galaxies (BLRG), 2 radio-quiet quasars (RQQ) and 1 radio-loud quasar (RLQ). In particular I focus on the nature of the warm absorber within this sample. The primary aim of this work is to present a uniform analysis of the *ASCA* data for a moderately large sample of type-1 AGN. Section 2 defines the sample and briefly describes the initial data reduction. The spectral fitting of the time-averaged *ASCA* spectra is detailed in Section 3 and the results are discussed in Section 4. It is found that all objects display some sign of spectral complexity indicating X-ray reprocessing phenomena are common. In particular, ionized absorption is detected with a high level of significance in 12 of the 24 objects. Since the dominant signatures of this absorption across the *ASCA* band are K-shell absorption edges due to O VII and O VIII, the absorption can be parameterised by the maximum optical depths of these edges. This provides the simplest parametrization of what is clearly a complex physical phenomenon. Relationships between these edge depths and other AGN properties (i.e. luminosity and optical reddening) are found. Section 5 presents the results of fitting the data with one-zone photoionization models as well as a comparison of these models with the simple two-edge fits. Spectral variability is briefly addressed in Section 6. After some notes on individual objects (Section 7), the general implications of these results on our understanding of the central engines of AGN are discussed (Section 8). My conclusions are presented in Section 9.

Throughout this paper it is assumed that $H_0 = 50 \text{ km s}^{-1} \text{ Mpc}^{-1}$ and $q_0 = 0$. Unless otherwise stated, errors on physical quantities are quoted at the 90 per cent confidence level for one interesting parameter ($\Delta\chi^2 = 2.7$). Error bars on plots are shown at the $1\text{-}\sigma$ level for one interesting parameter.

2 THE SAMPLE AND BASIC DATA REDUCTION

The sample consists of the 24 objects studied in the *EXOSAT* survey of Turner & Pounds (1989) and the *Ginga* survey of Nandra & Pounds (1994, hereafter NP94) for which *ASCA* data was publicly available at the time of the anal-

Table 1. The *ASCA* AGN sample. Column 2 indicates the type of nuclear activity (Sy1=Seyfert 1 galaxy; BLRG=broad-line radio galaxy; RLQ=radio-loud quasar; RQQ=radio-quiet quasar). Columns 3, 4 and 5 give the co-ordinates (J2000.0) and redshift of the source (from Veron-Cetty & Veron 1993). Column 6 gives the Galactic H I column density towards the source as determined by 21-cm measurements [^a indicates values obtained from Elvis, Lockman & Wilkes (1989) which are accurate to within 5 per cent; otherwise quoted values are interpolations from the measurements of Stark et al. (1992) and have uncertainties of $\sim 1 \times 10^{20} \text{ cm}^{-2}$]. Column 7 gives the start date of the *ASCA* observation used and column 8 gives the good exposure time for SIS0.

common source name	classification of activity	RA (J2000.0)	Decl (J2000.0)	redshift (z)	Galactic N_{H} (10^{20} cm^{-2})	start date	SIS0 Exp. (ks)
Mrk 335	Sy1	00 06 19.4	20 12 11	0.025	4.0	1993-Dec-9	19
Fairall 9	Sy1	01 23 45.7	-58 48 21	0.046	3.0	1993-Nov-21	22
Mrk 1040	Sy1	02 28 14.4	31 18 41	0.016	7.07 ^a	1994-Aug-19	19
3C 120	BLRG	04 33 11.0	05 21 15	0.033	12.32 ^a	1994-Feb-17	45
NGC 2992	Sy1	09 45 41.9	-14 19 35	0.008	5.56 ^a	1994-May-6	28
NGC 3227	Sy1	10 23 30.5	19 51 55	0.003	2.2	1993-May-8	47
NGC 3516	Sy1	11 06 47.4	72 34 06	0.009	3.4	1994-Apr-2	28
NGC 3783	Sy1	11 39 01.7	-37 44 18	0.009	3.7	1993-Dec-19	16
NGC 4051	Sy1	12 03 09.5	44 31 52	0.002	1.31 ^a	1993-Apr-25	27
3C 273	RLQ	12 29 06.6	02 03 08	0.158	3.0	1993-Dec-20	11
NGC 4593	Sy1	12 39 39.3	-05 20 39	0.009	1.97 ^a	1994-Jan-9	29
MCG-6-30-15	Sy1	13 35 53.3	-34 17 48	0.008	4.06 ^a	1994-Jul-23	147
IC 4329a	Sy1	13 49 19.2	-30 18 34	0.016	4.55 ^a	1993-Aug-15	33
NGC 5548	Sy1	14 17 59.5	25 08 12	0.017	1.7	1993-Jul-27	27
Mrk 841	RQQ	15 04 01.1	10 26 16	0.036	2.23 ^a	1994-Feb-21	21
Mrk 290	Sy1	15 35 52.2	57 54 08	0.030	2.32 ^a	1994-Jun-16	40
3C 382	BLRG	18 35 03.3	32 41 46	0.059	7.4	1994-Apr-18	36
3C 390.3	BLRG	18 42 08.7	79 46 16	0.057	4.1	1993-Nov-16	39
ESO 141-G55	Sy1	19 21 14.2	-58 40 12	0.037	5.5	1994-Sep-21	10
NGC 6814	Sy1	19 42 40.5	-10 19 24	0.006	9.80 ^a	1993-May-4	45
Mrk 509	Sy1	20 44 09.6	-10 43 23	0.035	4.2	1994-Apr-29	39
MR 2251-178	RQQ	22 54 05.7	-17 34 54	0.068	2.8	1993-Nov-6	7
NGC 7469	Sy1	23 03 15.5	08 52 26	0.017	4.82 ^a	1993-Nov-24	12
Mrk 926	Sy1	23 04 43.4	-08 41 08	0.047	4.6	1993-May-25	30

ysis (late 1995). Table 1 defines the sample. It contains 20 radio-quiet AGN (18 Seyfert 1 galaxies and 2 RQQ) and 4 radio-loud objects (3 BLRG and 1 RLQ). This sample is not homogeneous or complete in any well defined sense. However, it should be unbiased with respect to any of the spectral properties discussed in this paper. Indeed, the two lists from which the sample objects are drawn were compiled prior to any detailed knowledge of AGN spectral complexity.

Data from both the SIS and gas imaging spectrometers (GIS) were used. SIS data from both BRIGHT and FAINT mode were combined in order to maximize the total signal and a standard GRADE selection was performed in order to reduce the effects of particle and instrumental background. Data from the SIS were further cleaned in order to remove the effects of hot and flickering pixels and subjected to the following data-selection criteria:

- i) the satellite should not be in the South Atlantic Anomaly (SAA),
- ii) the object should be at least 5° above the Earth's limb,
- iii) the object should be at least 25° above the day-time Earth limb,
- iv) the local geomagnetic cut-off rigidity (COR) should be greater than 6 GeV/c.

Data from the GIS were cleaned to remove the particle background and subjected to the following data-selection criteria:

- i) the satellite should not be in the SAA,

- ii) the object should be at least 7° above the Earth's limb and

- iii) the COR should be greater than 7 GeV/c.

SIS and GIS data that satisfy these criteria shall be referred to as 'good' data.

Images, lightcurves and spectra were extracted from the good data using a circular region centred on the source. For the SIS, an extraction radius of 3 arcmins is used whereas a radius of 4 arcmins is used for the GIS. These regions are sufficiently large to contain all but a negligible portion of the source counts[†]. Background spectra were extracted from source free regions of the same field of view within each of the four *ASCA* instruments. Background regions for the SIS were taken to be rectangular regions along the edges of the source chip whereas annular regions were used to extract GIS background.

The data reduction described in the previous paragraphs was performed using version 1.3 of the XSELECT program contained within the FTOOLS software package.

3 SPECTRAL ANALYSIS

[†] See point spread function in the '*ASCA* Technical Description', Appendix E of the *ASCA* Research Announcement

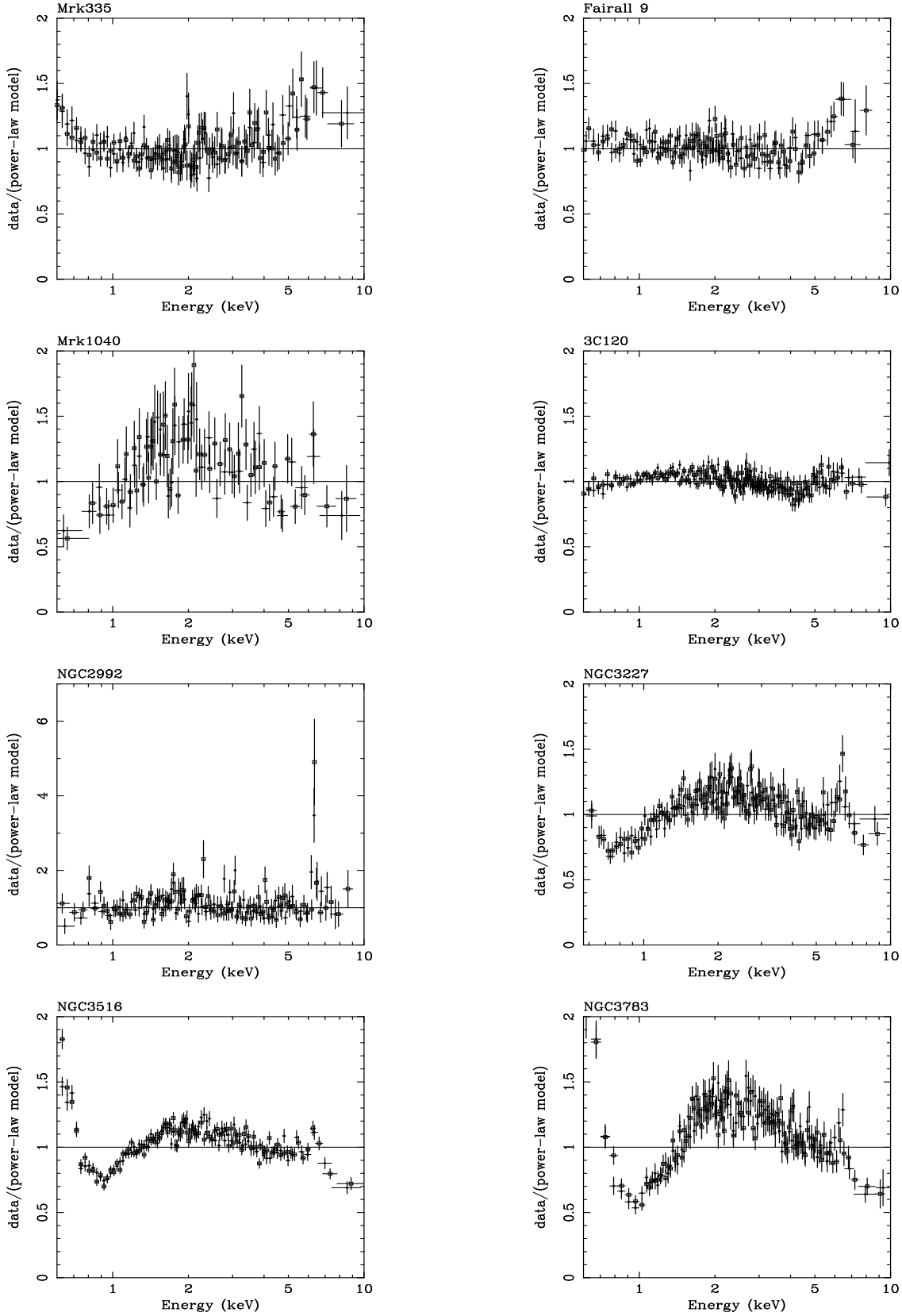


Figure 1.

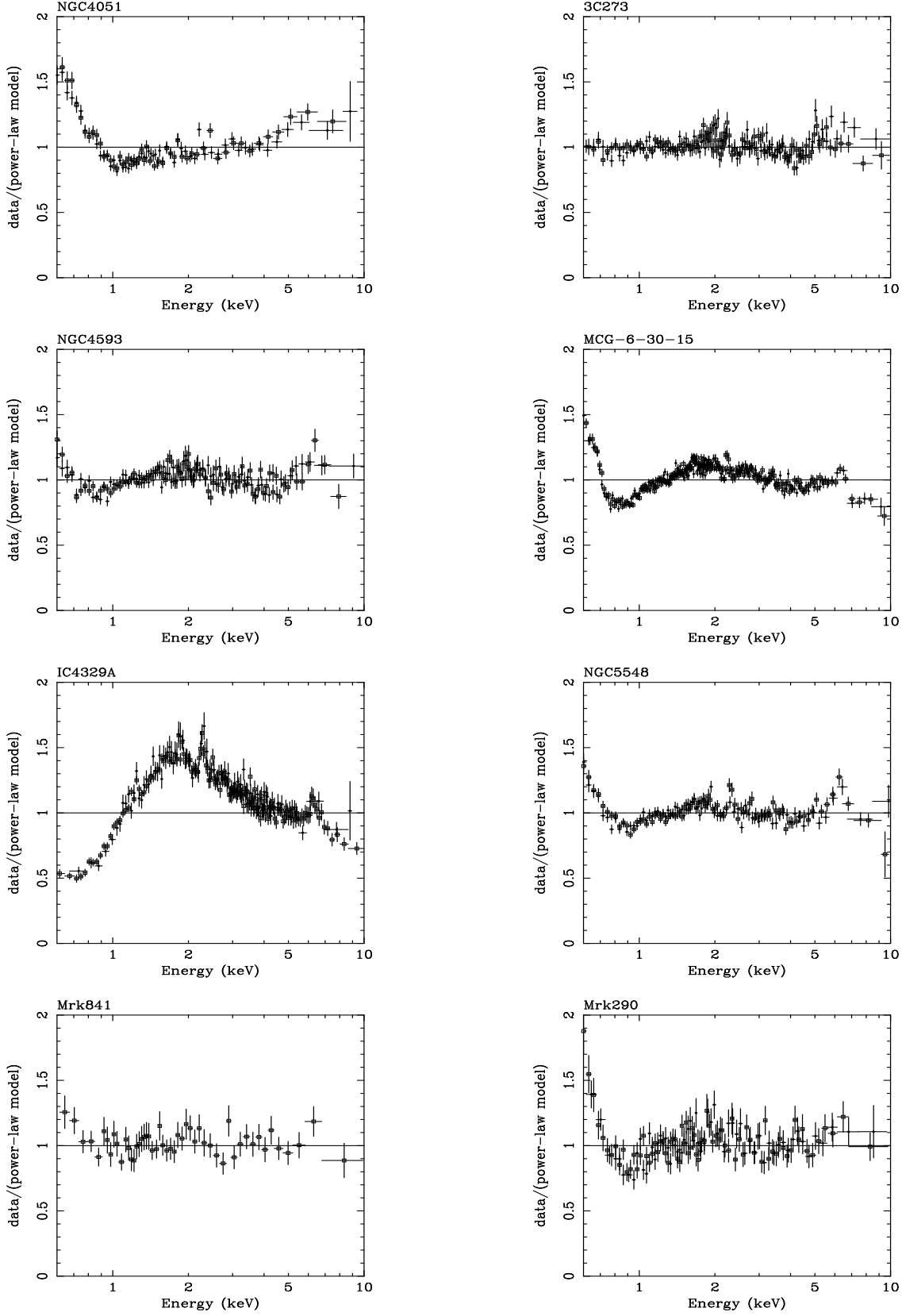


Figure 1. cont.

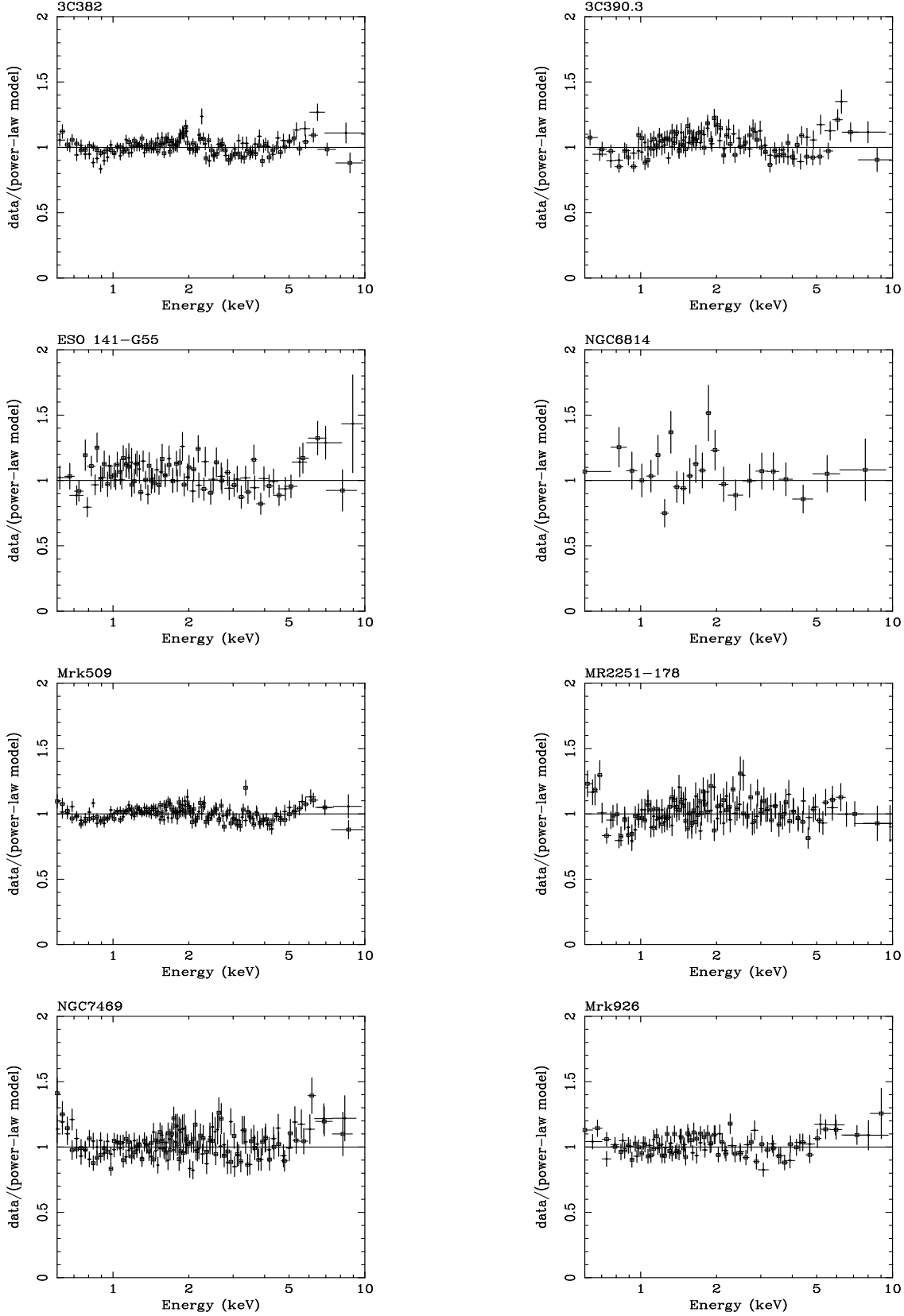


Figure 1. cont. Ratio of the data to the best fit power-law modified by cold Galactic absorption (model-A). All 4 instruments were used for spectral fitting but only SIS data are shown in order to maintain clarity. Open squares are the SIS0 data whereas plain crosses are the SIS1 data. See text for a full discussion.

Table 2. Spectral fitting results for model-A (power-law modified by Galactic absorption). Column 2 gives the average SIS0 count rate for the good data. Columns 3 and 4 show the 2–10 keV flux and luminosity, respectively, for these best fit power-law models (*with no correction for the effects of absorption applied*). Column 5 shows the best fit power-law photon index. Column 6 shows the goodness of fit and the number of degrees of freedom (dof). All errors are quoted at the 90 per cent confidence level for one interesting parameter ($\Delta\chi^2 = 2.7$) apart from the error on the average SIS0 count rate, which is quoted at the 1- σ level for one interesting parameter ($\Delta\chi^2 = 1.0$).

source name	SIS0 count rate (cts s ⁻¹)	F_{2-10} (10 ⁻¹² erg cm ⁻² s ⁻¹)	L_{2-10} (10 ⁴³ erg s ⁻¹)	Photon index Γ	χ^2/dof
Mrk 335	0.677 ± 0.006	9.2	2.5	2.17 ± 0.01	899/741
Fairall 9	1.001 ± 0.007	19.0	18	1.93 ± 0.01	1283/1149
Mrk 1040	0.121 ± 0.003	5.4	0.60	1.20 ± 0.03	530/371
3C 120	1.858 ± 0.007	45.5	22	1.85 ± 0.01	1894/1051
NGC 2992	0.082 ± 0.002	4.1	0.11	1.06 ± 0.04	516/439
NGC 3227	0.641 ± 0.006	23.3	0.09	1.30 ± 0.01	2294/1487
NGC 3516	2.497 ± 0.010	78	2.7	1.47 ± 0.01	3692/1041
NGC 3783	1.080 ± 0.009	54	1.9	0.92 ± 0.1	3894/1319
NGC 4051	1.049 ± 0.006	16	0.03	2.14 ± 0.01	3641/1342
3C 273	4.731 ± 0.022	131	1530	1.59 ± 0.01	1537/1476
NGC 4593	1.660 ± 0.008	35	1.2	1.84 ± 0.01	1672/1391
MCG-6-30-15	1.905 ± 0.004	46	1.3	1.70 ± 0.01	8804/2400
IC 4329a	2.896 ± 0.009	78	8.6	1.30 ± 0.01	16000/1781
NGC 5548	2.501 ± 0.010	43	5.4	1.79 ± 0.01	2330/1633
Mrk 841	0.359 ± 0.004	10	5.7	1.63 ± 0.03	334/331
Mrk 290	0.321 ± 0.003	9.1	3.6	1.61 ± 0.02	1168/1017
3C 382	1.944 ± 0.008	41	64	1.89 ± 0.01	1722/1452
3C 390.3	0.551 ± 0.004	17	24	1.59 ± 0.01	1475/1251
ESO 141-G55	0.716 ± 0.009	17	10	1.79 ± 0.02	816/725
NGC 6814	0.044 ± 0.001	1.1	0.017	1.61 ± 0.07	267/258
Mrk 509	2.095 ± 0.008	44	24	1.87 ± 0.01	1676/1500
MR 2251-178	1.817 ± 0.017	45	93	1.65 ± 0.02	871/846
NGC 7469	1.453 ± 0.011	29	3.6	2.02 ± 0.01	1052/986
Mrk 926	0.613 ± 0.005	14	14	1.73 ± 0.02	1106/1004

3.1 Initial Spectral fitting

Initially I fitted the time-average spectrum of each object with a model consisting of a power-law (with photon index Γ) modified by Galactic absorption (as determined from H I 21-cm measurements and quoted in Table 1). This will be denoted as *model-A*. Where available, data from all four *ASCA* instruments were fitted simultaneously. SIS data between 0.5–10 keV and GIS data between 0.8–10 keV were used. The data were rebinned so that each spectral bin contained at least 20 counts. Background subtracted spectra were then fitted using the standard χ^2 minimization technique implemented in version 9.00 of the XSPEC spectral fitting package. Table 2 gives the results of these fits. Figure 1 shows the ratio of the SIS data with the best-fitting power-law spectrum.

It is clear from Table 2 and Figure 1 that model-A is a poor description of the data for many of the objects. Several objects show low-energy excesses characteristic of the so-called soft-excess (with clear examples being Mrk 335, NGC 4051 and Mrk 841), many display a ‘notch’ between ~ 0.7 –2 keV which is the signature of a warm-absorber (e.g. NGC 3227, NGC 3516, NGC 3783, NGC 4593, MCG-6-30-15, NGC 5548, Mrk 290 and MR 2251-178) and almost all objects have an excess at energies characteristic of iron K α line emission. The instrumental feature at 2.2 keV (due to the M-shell absorption edge of the gold coating the X-ray mirrors) can also be seen in many of the

objects. The effect of this feature on the statistics of the spectral fitting described here is negligible.

3.2 Phenomenological model

A more complex model is required in order to explore the various spectral features displayed by these data. Therefore, to the spectrum of each object was fitted a spectral model consisting of the following components:

- (i) a power-law representing the primary continuum (photon index Γ).
- (ii) Gaussian emission line representing iron K α emission (energy E , width σ and equivalent width W_{Fe} in the rest-frame of the source).
- (iii) two absorption edges with rest-frame threshold energies of 0.74 keV representing O VII and 0.87 keV representing O VIII K-shell absorption (with maximum optical depths τ_{O7} and τ_{O8}) respectively. These two edges provide, to a good approximation, a description of the effects of the warm absorber over the *ASCA* band. A comparison of this two-edge model to a more complete photoionization model will be performed in Section 5.
- (iv) intrinsic absorption by a column density N_{H} of neutral matter in the rest-frame of the source. This absorbing material is assumed to have cosmic abundances.
- (v) Galactic absorption (at $z = 0$) fixed at the level determined by the H I 21-cm measurements reported in Table 1.

Table 3. Absorption results from spectral fitting with model-B, as defined in Section 3.2 of the main text. Column 6 gives the intrinsic (i.e. corrected for all forms of absorption) 2–10 keV luminosity. Uncertainties on these luminosities are ~ 5 per cent and are dominated by instrumental systematics. Column 7 gives the goodness of fit parameter. Column 8 reports the improvement in χ^2 upon the addition of the oxygen absorption edges ($\Delta\chi^2 > 9\chi^2_{\nu}$ for 2 additional degrees of freedom corresponds to an improvement at the 99 per cent confidence level) if only data above 0.6 keV is considered. All errors and limits are quoted at the 90 per cent confidence level for one interesting parameter ($\Delta\chi^2 = 2.7$).

source name	Photon Index Γ	Intrinsic N_{H} (10^{20} cm^{-2})	O VII edge depth, $\tau_{\text{O}7}$	O VIII edge depth, $\tau_{\text{O}8}$	L_{2-10} ($10^{43} \text{ erg s}^{-1}$)	χ^2/dof	$\Delta\chi^2$ upon adding edges
Mrk 335	$2.07^{+0.07}_{-0.06}$	< 0.9	0.27 ± 0.11	< 0.09	2.79	678/735	11
Fairall 9	$1.99^{+0.02}_{-0.03}$	$1.2^{+0.8}_{-0.7}$	< 0.01	< 0.03	18.0	1219/1143	0
Mrk 1040	$1.69^{+0.09}_{-0.07}$	$2.2^{+0.8}_{-0.7}$	$0.41^{+0.50}_{-0.41}$	$0.24^{+0.50}_{-0.24}$	0.566	352/361	2
3C 120	$2.08^{+0.07}_{-0.03}$	$8.2^{+1.0}_{-0.6}$	< 0.01	< 0.05	21.4	1106/1045	0
NGC 2992	$1.25^{+0.09}_{-0.07}$	$8.5^{+4.5}_{-4.0}$	< 0.19	$0.21^{+0.44}_{-0.21}$	0.112	447/433	3
NGC 3227	1.57 ± 0.02	9.5 ± 1.3	$0.53^{+0.11}_{-0.10}$	$0.18^{+0.08}_{-0.07}$	0.089	1497/1481	60
NGC 3516	$1.72^{+0.02}_{-0.01}$	$0.2^{+0.6}_{-0.2}$	0.80 ± 0.05	$0.40^{+0.05}_{-0.04}$	2.64	1188/1035	1477
NGC 3783	$1.43^{+0.02}_{-0.03}$	4.6 ± 0.9	1.2 ± 0.1	1.4 ± 0.1	1.77	1562/1371	785
NGC 4051	$2.04^{+0.03}_{-0.02}$	< 0.6	0.19 ± 0.06	$0.23^{+0.04}_{-0.05}$	0.0289	1479/1335	102
3C 273	$1.66^{+0.01}_{-0.02}$	$1.9^{+0.6}_{-0.5}$	$0.01^{+0.05}_{-0.01}$	$0.07^{+0.04}_{-0.03}$	1530	1482/1470	9
NGC 4593	1.97 ± 0.03	$2.0^{+0.5}_{-0.6}$	0.26 ± 0.04	$0.09^{+0.04}_{-0.03}$	1.23	1418/1385	123
MCG-6-30-15	$1.92^{+0.02}_{-0.01}$	$1.7^{+0.4}_{-0.3}$	0.64 ± 0.02	$0.19^{+0.02}_{-0.03}$	1.23	3020/2394	3336
IC 4329a	1.85 ± 0.02	$30.8^{+0.09}_{-0.10}$	0.59 ± 0.07	0.12 ± 0.05	8.80	2201/1779	123
NGC 5548	1.88 ± 0.01	< 0.22	$0.25^{+0.04}_{-0.04}$	0.16 ± 0.03	5.44	1727/1627	310
Mrk 841	$1.64^{+0.08}_{-0.06}$	< 10	$0.18^{+0.28}_{-0.18}$	$0.03^{+0.20}_{-0.03}$	5.89	300/325	0
Mrk 290	$1.77^{+0.03}_{-0.02}$	< 0.60	0.37 ± 0.09	$0.33^{+0.08}_{-0.07}$	3.76	937/1011	107
3C 382	$2.02^{+0.06}_{-0.03}$	$1.1^{+1.2}_{-0.8}$	0.16 ± 0.05	0.10 ± 0.04	65.3	1588/1446	41
3C 390.3	$1.74^{+0.07}_{-0.04}$	$5.8^{+1.5}_{-0.9}$	$0.09^{+0.07}_{-0.08}$	$0.07^{+0.07}_{-0.06}$	23.7	1303/1245	18
ESO 141-G55	$1.90^{+0.03}_{-0.04}$	$5.2^{+1.5}_{-1.2}$	< 0.03	< 0.02	9.89	759/719	0
NGC 6814	$1.65^{+0.18}_{-0.09}$	< 5.8	< 0.25	$0.05^{+0.33}_{-0.05}$	0.0178	261/252	0
Mrk 509	1.98 ± 0.02	2.1 ± 0.6	$0.11^{+0.03}_{-0.04}$	$0.04^{+0.04}_{-0.03}$	23.9	1549/1494	33
MR 2251-178	$1.73^{+0.02}_{-0.03}$	< 0.6	0.32 ± 0.10	0.15 ± 0.08	93.2	764/840	83
NGC 7469	$2.11^{+0.04}_{-0.03}$	< 0.4	$0.17^{+0.08}_{-0.07}$	$0.03^{+0.05}_{-0.03}$	3.69	963/980	13
Mrk 926	$1.80^{+0.05}_{-0.04}$	< 1.5	$0.06^{+0.08}_{-0.06}$	$0.04^{+0.07}_{-0.04}$	13.9	1055/998	3

This will be denoted as *model-B*. The model was fitted simultaneously to the background subtracted spectra from each of the four *ASCA* instruments for each object of the sample. Free parameters in the fit were Γ , E , σ , W_{Fe} , $\tau_{\text{O}7}$, $\tau_{\text{O}8}$ and N_{H} . The normalizations of the model for each of the four instruments were also left as free parameters. This allows for the ~ 10 –20 per cent uncertainties between the normalizations of the different instruments.

Aspects of this model require justification. First, although we include the fluorescent iron-line emission, the associated reflection continuum is not included. In the ‘standard’ case of reflection by a cold slab of material covering a solid angle of 2π as seen by the X-ray source, we expect a negligible effect in the *ASCA* band [e.g. see Monte-Carlo simulations of George & Fabian (1991) and Reynolds, Fabian & Inoue (1995).] Objects with a stronger reflection continuum due to, for example, time-delayed reflection from the molecular torus after the central source has faded (e.g. IC 4329a, Cappi et al. 1996; NGC 2992, Weaver et al. 1996) might be expected to display an unmodelled hard tail once they have been fitted with model-B. Secondly, the energies of the two absorption edges have been fixed at the physical rest-frame energies of the K-shell absorption edges of O VII and O VIII (0.74 keV and 0.87 keV respectively) as opposed to allowing the threshold energies to vary as free parameters in the fit. This method is the most robust to the

various unmodelled spectral complexities such as recombination line/continuum emission, resonance absorption lines and other absorption edges. These complexities would require many additional degrees of freedom to model (such as the covering fraction of the warm material, its density, the chemical abundances and the velocity structure) and would lead to an over modelling of the data for all but the very highest quality *ASCA* data. In fitting a simple two-edge model, these complexities could lead to false shifts in the threshold edge energies of the edges (for example, see the discussion of MCG-6-30-15 in Section 5.2). An independent reason for fixing the edge energies is to allow us to compare objects that show warm absorption and those that do not show any evidence for warm absorption (i.e. only have upper limits for the edge depths).

After fitting this model to the sample, three objects (Mrk 335, NGC 4051 and Mrk 841) display residues clearly demonstrating the need for a soft-excess component. Thus, for these objects an additional black-body component (also subject to the same cold and ionized absorption as the power-law continuum) is added to the model in order to take account of the soft excess. A more systematic study of the presence of soft excesses in the rest of the sample will be performed in the Section 4.4.

Table 3 reports the results for the absorption features of spectral fitting with model-B. Table 4 reports the iron-line

Table 4. Iron emission line results from spectral fitting with model-B, as defined in Section 3.2 of the main text. Given here are the best fitting energies E , widths σ (defined as the normal deviation of the emission profile) and equivalent widths W_{Fe} . For ESO 141-G55 the line energy and width had to be fixed (as indicated by the ‘f’) in order to avoid a disastrous statistical degeneracy. All errors and limits are quoted at the 90 per cent confidence level for one interesting parameter ($\Delta\chi^2 = 2.7$).

object name	E (keV)	σ (keV)	W_{Fe} (eV)	$\Delta\chi^2$ upon allowing line to be broad
Mrk 335	6.1 ± 0.4	$0.89^{+0.80}_{-0.34}$	560^{+600}_{-260}	15
Fairall 9	$6.37^{+0.11}_{-0.13}$	$0.45^{+0.26}_{-0.17}$	380^{+150}_{-100}	22
Mrk 1040	$6.37^{+0.12}_{-0.10}$	$0.25^{+0.15}_{-0.13}$	480^{+260}_{-130}	5
3C 120	$6.43^{+0.23}_{-0.24}$	$1.5^{+0.6}_{-0.4}$	960^{+520}_{-270}	119
NGC 2992	6.41 ± 0.02	< 0.06	560^{+110}_{-130}	0
NGC 3227	6.34 ± 0.07	$0.24^{+0.12}_{-0.08}$	210^{+80}_{-40}	29
NGC 3516	$6.41^{+0.05}_{-0.06}$	$0.12^{+0.10}_{-0.06}$	120^{+30}_{-40}	7
NGC 3783	6.42 ± 0.03	0.04 ± 0.04	130 ± 30	1
NGC 4051	$5.87^{+0.24}_{-0.23}$	$0.82^{+0.28}_{-0.23}$	400^{+160}_{-130}	18
3C 273	$6.78^{+0.27}_{-0.26}$	$0.78^{+0.24}_{-0.20}$	200^{+70}_{-60}	30
NGC 4593	6.43 ± 0.15	$0.66^{+0.22}_{-0.20}$	410 ± 120	22
MCG-6-30-15	6.05 ± 0.08	$0.59^{+0.09}_{-0.08}$	220 ± 40	133
IC 4329a	$6.39^{+0.08}_{-0.10}$	$0.44^{+0.15}_{-0.13}$	270^{+100}_{-60}	62
NGC 5548	6.37 ± 0.11	$0.49^{+0.20}_{-0.14}$	280^{+90}_{-70}	39
Mrk 841	$6.46^{+0.14}_{-0.30}$	$0.15^{+0.42}_{-0.15}$	120^{+110}_{-70}	1
Mrk 290	$6.27^{+0.15}_{-0.16}$	$0.47^{+0.18}_{-0.14}$	420 ± 120	41
3C 382	$6.44^{+0.32}_{-0.44}$	$1.8^{+1.0}_{-0.5}$	900^{+1042}_{-310}	75
3C 390.3	$6.46^{+0.17}_{-0.11}$	0.39 ± 0.18	300^{+440}_{-90}	17
ESO 141-G55	6.4^{f}	0.1^{f}	140 ± 70	–
NGC 6814	$6.46^{+0.38}_{-0.37}$	< 0.9	430^{+800}_{-300}	0
Mrk 509	$6.64^{+0.24}_{-0.21}$	$1.27^{+0.34}_{-0.31}$	680^{+230}_{-190}	69
MR 2251-178	$6.1^{+0.4}_{-0.3}$	$0.53^{+0.52}_{-0.26}$	190^{+140}_{-90}	8
NGC 7469	$6.56^{+0.29}_{-0.26}$	$1.19^{+0.56}_{-0.36}$	1000^{+400}_{-280}	46
Mrk 926	$6.27^{+0.29}_{-0.25}$	$0.84^{+0.42}_{-0.45}$	540^{+300}_{-220}	47

results. Model-B (with the addition of soft excesses in the case of Mrk 335, NGC 4051 and Mrk 841) provides a good description of the data for most objects.

4 RESULTS

4.1 The primary X-ray continuum

The photon index of the primary X-ray continuum is a crucial observational constraint on our understanding of high-energy radiation mechanisms associated with the inner accretion flow. If we assume that model-B correctly accounts for all X-ray reprocessing phenomena relevant in the *ASCA* band, the best fitting value of Γ should represent the photon index of the primary continuum. Figure 2 shows the distribution of derived photon indices for this sample. The photon index distribution for the sample as a whole has mean $\langle\Gamma\rangle = 1.81$ and dispersion $\sigma_{\Gamma} = 0.21$. The distributions for the radio-loud and radio-quiet sub-samples have $\langle\Gamma\rangle = 1.88$ (dispersion $\sigma_{\Gamma} = 0.18$) and $\langle\Gamma\rangle = 1.80$ (dispersion $\sigma_{\Gamma} = 0.21$) respectively. Thus the photon indices of the radio-loud and radio-quiet sub-samples do not appear to be significantly different, although the number of radio-loud objects is small.

4.2 Ionized absorption

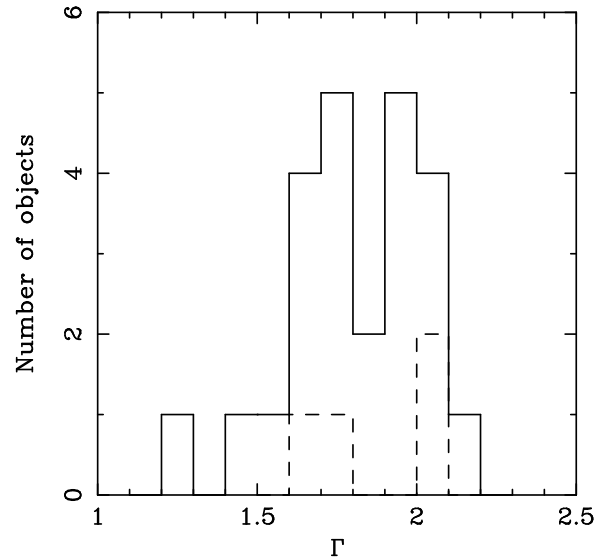


Figure 2. Distribution of photon indices derived from model-B, as defined in Section 3.2 of the main text. The solid line shows the distribution of the whole sample whereas the dashed lines shows the contribution to this from the four radio-loud objects.

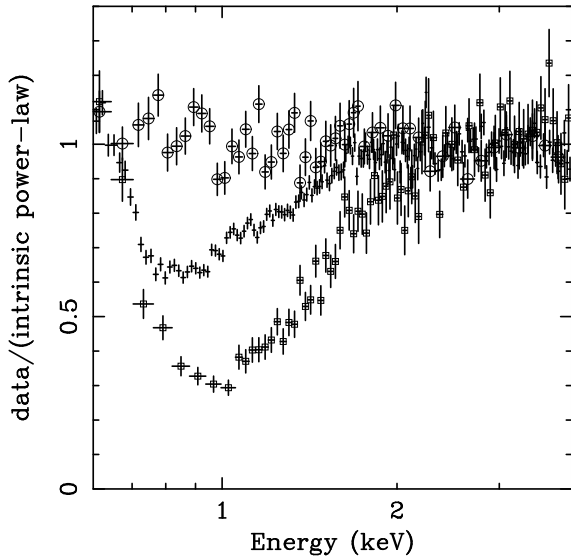


Figure 3. Ratio of the data for three objects to the intrinsic power-law spectrum (modified by neutral Galactic absorption) inferred from spectral fitting with model-B. The objects are Fairall 9 (top dataset, large circles), MCG-6-30-15 (middle dataset, plain crosses) and NGC 3783 (bottom dataset, small squares). The deep ionized oxygen edges can be clearly seen in both MCG-6-30-15 and NGC 3783. By contrast, Fairall-9 shows no deviation from the intrinsic spectrum (implying no soft X-ray reprocessing). No correction for redshift has been applied to the observed energies.

4.2.1 Ubiquity of the warm absorber

An important result of the spectral fitting reported in Table 3 is the frequency with which statistically-significant ionized absorption is detected (as indicated by statistically-significant oxygen absorption edges). 12 out of the 24 objects show a significant improvement in the goodness of fit (according to the F-test using a 99 per cent confidence level; Bevington 1969) when the two oxygen edges are included. Such a harsh statistical criterion was used to protect against any small calibration uncertainties. These objects are listed in Table 6 (see Section 5 for a full discussion of Table 6). This result is robust to neglecting all data below 0.6 keV. The result is also unaffected if we include the possibility of a black body soft excess in the spectral fitting (see Section 4.4). The effect of the ionized absorption is demonstrated in Fig. 3. Here we show the ratio of the data to the inferred underlying power-law continuum (corrected for neutral absorption) for Fairall-9 (which displays no significant warm absorption), MCG-6-30-15 (which shows strong evidence for ionized absorption) and NGC 3783 (which shows the deepest ionized absorption edges of all the sources in the present sample). Note the sharp onset of absorption at ~ 0.7 keV and the gradual recovery over the 1-2 keV range.

This sample has sufficient sources to search for general trends. Figure 4 shows the warm oxygen edge depths as a function of luminosity for the sample. Whilst there is no clear correlation of τ_{O7} or τ_{O8} with luminosity, there does appear to be a luminosity-dependent upper envelope to these

distributions such that there are no high-luminosity systems displaying deep edges. To formally address this, the full sample of 24 objects was divided into a high luminosity half and a low luminosity half (on the basis of the 2-10 keV luminosities derived from model-B fits and reported in Table 3). The distribution of τ_{O7} and τ_{O8} in each of these subsamples were compared using a KS test. The high- L and low- L distributions of τ_{O7} are found to be inconsistent at the 95 per cent level (i.e. there is only a 5 per cent probability that the two distributions were drawn from the same parent distribution). A much stronger result is obtained for the high- L and low- L distributions of τ_{O8} : these are found to be inconsistent at the 99.5 per cent level (i.e. only a 0.5 per cent probability that the two distributions were drawn from the same parent distribution).

Care must be exercised in the physical interpretation of this result since the four radio-loud objects are amongst the most luminous of the sample. Performing the same statistical analysis on the radio-quiet subsample only, no significant relationship between the ionized edge depths and luminosity is found. Thus, the underlying dependence is unclear: the apparent luminosity relationship of the previous paragraph may be a manifestation of a true dependence of the ionized absorption on radio-loudness. The present dataset is too small to disentangle the effects of any true luminosity dependence from any dependence based on radio properties. A detailed spectral examination of low-luminosity radio-loud objects or high luminosity radio quiet objects would be necessary to settle this issue.

4.2.2 Ionized absorption and the optical/UV properties

Recent evidence has emerged linking the ionized absorption seen in the X-ray spectrum of AGN with optical/UV characteristics of the objects. Firstly, it has been suggested that the UV absorption lines seen in the broad line profiles of many AGN arise from the same ionized material as do the warm absorption features (Mathur et al. 1994; Mathur 1994; Mathur, Elvis & Wilkes 1995). Given this identification, the velocity structure of the absorbing material can be accurately measured from the UV absorption lines. Mathur, Elvis & Wilkes (1995) examine the Seyfert 1 galaxy NGC 5548 and deduce that the absorber forms an outflow with a velocity of $1200 \pm 260 \text{ km s}^{-1}$.

There is also strong evidence that at least some warm absorbers are intrinsically dusty leading to a connection between optical/UV reddening and ionized absorption. The two strongest cases are MCG-6-30-15 (Reynolds & Fabian 1995) and IRAS 13349+2438 (Brandt, Fabian & Pounds 1996). Both of these objects display significant optical reddening ($E(B-V) \gtrsim 0.3$) which, assuming a Galactic dust-to-gas ratio implies a line-of-sight gas column density in excess of $2 \times 10^{21} \text{ cm}^{-2}$ (Burstein & Heiles 1978). However, both of these objects have tight X-ray limits on the amount of neutral gas which are inconsistent with the reddening value by an order of magnitude or more (i.e. the X-ray limits are $N_H \lesssim 2 \times 10^{20} \text{ cm}^{-2}$). A resolution of this apparent discrepancy, which avoids postulating ad-hoc geometries or exceptionally high dust-to-gas ratios, is to place the dust responsible for the reddening in the warm ionized material inferred from the oxygen edges seen in the X-ray spectrum of these two objects.

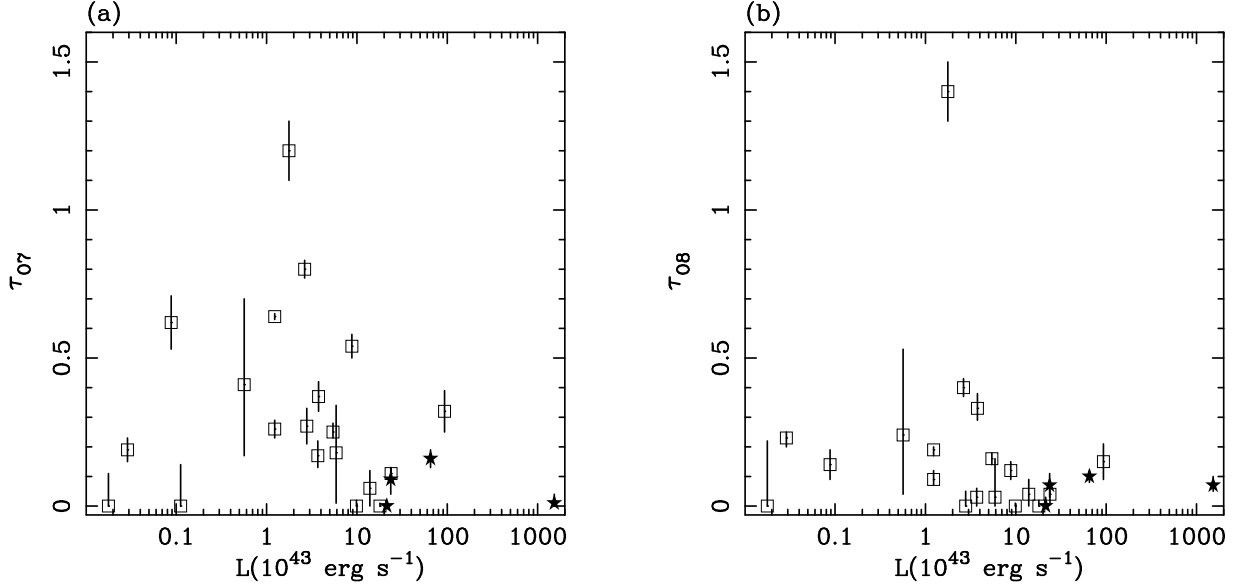


Figure 4. Maximum oxygen edge depth (τ_{O7} and τ_{O8}) as a function of (unabsorbed) 2–10 keV X-ray luminosity, L . Squares represent data points for radio-quiet objects whereas stars show the radio-loud data points. Panel (a) reports the threshold optical depth of the O VII edge as a function of L . Whilst there is no formal correlation present, there is a dearth of high luminosity systems also showing a large O VII edge. This is discussed in the text. Panel (b) shows the threshold optical depth of the O VIII edge as a function of L . A similar dependence is seen. Errors are displayed at the 1- σ level for one interesting parameter.

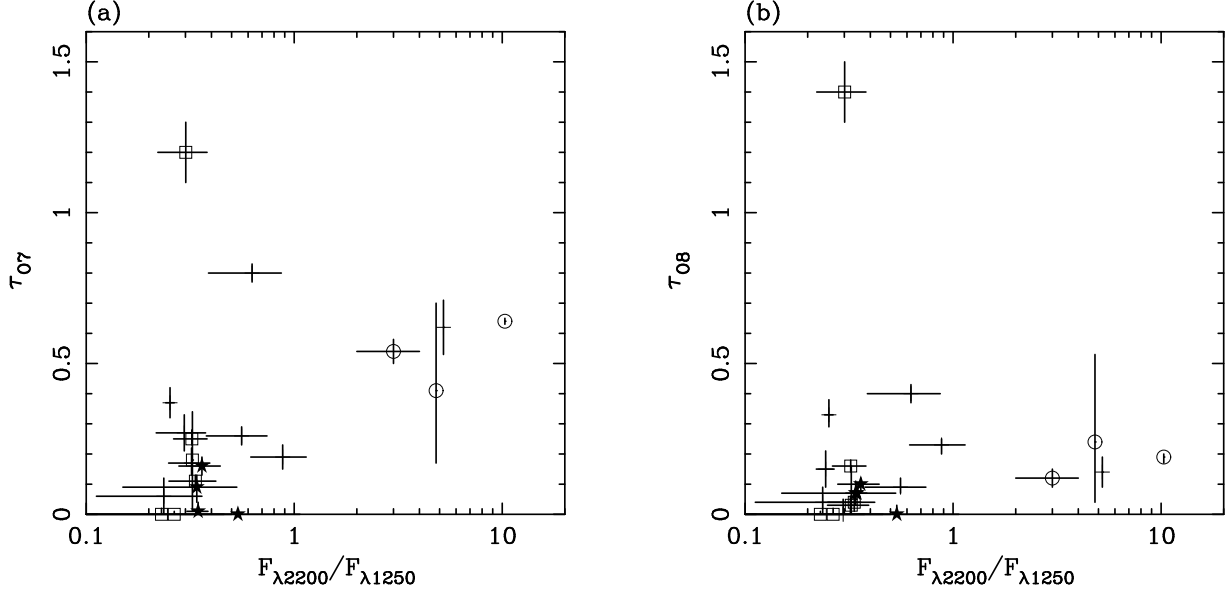


Figure 5. Maximum oxygen edge depth (τ_{O7} and τ_{O8}) as function of a reddening indicator, X , given by the ratio of the continuum flux at 2200Å and 1250Å. Squares show those objects classified by Ward et al. (1987) to be ‘bare’ (unreddened) whereas circles denote those objects classified as heavily reddened. Note the agreement between Ward et al. and the reddening indicator used here. Stars show the data for the radio-loud objects of the sample. Trends are discussed in the text. Errors are shown at the 1- σ level for one interesting parameter.

Dust can survive in warm ionized plasma given that two conditions are satisfied. Firstly, the *gas* must be below the temperature at which sputtering will destroy the dust ($T \sim 10^6$ K). Since the warm gas is photoionization dominated, the required high ionization states can easily be achieved without exceeding this temperature (see Section 5 for photoionization models). Turning this argument around, we can cite observations of highly-ionized dusty gas as supporting evidence for the hypothesis that this gas is photoionization dominated. Secondly, the *dust* must be below its sublimation temperature ($T \sim 1000\text{--}2000$ K depending on the exact dust grain type under consideration). It is important to note that the grain temperature can differ greatly from the gas temperature due to the tenuous nature of the gas. In fact, to a good approximation, the grains near the central engine of an AGN will be in thermal equilibrium with the primary radiation field. Assuming that each grain radiates as a black body, the temperature, T , of the grains can be estimated by equating the radiative flux incident on the grain from the primary source with the black body radiation emitted by the grain. This gives

$$T = \left(\frac{L_B}{16\pi\sigma R^2} \right)^{1/4}, \quad (1)$$

where σ is the Stefan-Boltzmann constant and R is the distance from an (isotropic) source with bolometric luminosity L_B . If $L_B = 10^{44} L_{44} \text{ erg s}^{-1}$ and $R = R_{\text{pc}} \text{ pc}$, this evaluates to give

$$T = 250 L_{44}^{1/4} R_{\text{pc}}^{-1/2} \text{ K} \quad (2)$$

Thus, for typical Seyfert luminosities ($L_{44} \sim 1$), dust can survive in the warm gas provided it is more than $\sim 10^{17}$ cm from the primary source.

Motivated by these studies, it is interesting to search for a relationship between the optical/UV reddening and ionized absorption. A difficulty in such a study is to determine the reddening in a uniform manner across the sample. Determining reddening via Balmer decrements suffers from major uncertainties in the value of the intrinsic Balmer decrement of the various emission line regions. Radiative transfer effects can severely modify the Balmer decrements predicted from the simple case-B recombination (Kwan & Krolik 1981) values. Furthermore, determining reddening by comparing two wildly different wavebands (for example, UV and hard X-ray bands) is a poor technique for such a sample due to the lack of simultaneous multiwavelength observations of most sources and the variable nature of these sources. Here, I use a reddening indicator, X , defined as the ratio of the continuum flux at 2200\AA , $F_{\lambda 2200}$, to that at 1250\AA , $F_{\lambda 1250}$,

$$X = \frac{F_{\lambda 2200}}{F_{\lambda 1250}} \quad (3)$$

as determined by the International Ultraviolet Explorer (*IUE*) and reported in the AGN compilation of Courvoisier & Paltani (1992). Only quasi-simultaneous (i.e. same day) measurements of these two fluxes were considered in order to minimise the effects of source variability. For objects with more than one such quasi-simultaneous measurement, the mean and standard deviation of the various values of X were computed. For a given primary continuum shape, reddening will tend to increase X .

Figure 5 shows τ_{07} and τ_{08} as a function of the red-

dening indicator, X . To check that X does indeed distinguish reddened objects from unreddened objects, the classifications of Ward et al. (1987) have been used. It can be seen from Fig. 5 that those objects classified as reddened by Ward et al. (shown as open circles) have $X \gtrsim 3$ whereas those classified as unreddened (shown as open squares) have $X \lesssim 0.4$. Thus, X appears to be an excellent indicator of the reddening.

Trends are seen in the τ_{07} - X plot (Fig. 5a). In particular, three classes of objects can be distinguished: unreddened objects with small O VII edges, reddened objects with appreciable O VII edges and two outliers (NGC 3516 and NGC 3783) which have a small reddening and a very large O VII edge. To formally assess this trend, the sample was divided into an unreddened subsample (with $X < 1$) and a reddened subsample ($X > 1$). The distributions of τ_{07} for these two subsamples are inconsistent (according to a KS test) at more than the 99 per cent level. This result is independent of whether the radio-loud objects are included or not. No strong trends are seen in the τ_{08} - X plot (Fig. 5b) except that all reddened objects have non-zero O VIII edge depths.

The implications of these results for AGN models are discussed in Section 8.

4.3 Iron-line emission

All objects in the current sample show a statistically significant improvement in the goodness of fit upon the addition of a Gaussian emission line at energies characteristic of iron K α line emission. The resulting line properties for each object are shown in Table 4. 20 out of the 24 objects show a significantly broadened line (i.e. if the line is initially fixed to be narrow and the width is then introduced as a free parameter, 20 out of 24 objects demonstrate a significant improvement in the goodness of fit according to the F-test). In most cases this can be interpreted as fluorescent iron K α emission from the inner regions of an accretion disk: this hypothesis has been dramatically strengthened by the accurate line profile obtained with a long *ASCA* observation of MCG-6-30-15 (Tanaka et al. 1995; Fabian et al. 1995) which matches the model prediction.

Given that the broad iron emission originates from the central most regions of the accretion flow, comparing any such emission from radio-loud and radio-quiet nuclei should give important clues as to the fundamental differences between these two classes of objects. Although the number of radio-loud objects in the present sample is small (only 4), some interesting trends are suggested. For the radio-quiet objects alone, the distribution of line properties has $\langle E \rangle = 6.33 \text{ keV}$ (dispersion $\sigma_E = 0.18 \text{ keV}$), $\langle \sigma \rangle = 0.50 \text{ keV}$ (dispersion $\sigma_\sigma = 0.37 \text{ keV}$) and $\langle W_{\text{Fe}} \rangle = 380 \text{ eV}$ (dispersion $\sigma_W = 220 \text{ eV}$). The corresponding quantities for the four radio-loud objects are $\langle E \rangle = 6.53 \text{ keV}$ (dispersion $\sigma_E = 0.15 \text{ keV}$), $\langle \sigma \rangle = 1.12 \text{ keV}$ (dispersion $\sigma = 0.56 \text{ keV}$) and $\langle W_{\text{Fe}} \rangle = 590 \text{ eV}$ (dispersion $\sigma_W = 340 \text{ eV}$). Whilst the number of objects are small there is a clear trend for radio-loud objects to have features which are broader than those in radio-quiet objects. There may also be a suggestive trend of higher centroid energies and larger equivalent widths in the radio-louds. This maybe related to the presence of a relativistic jet in the radio loud objects (3C 120 and 3C 273

Table 5. Best-fitting soft excess parameters for objects showing a statistically significant improvement (at the 99 per cent level) upon addition of a black body component. Column 2 gives the best-fitting black body temperature with errors shown at the 90 per cent level for one interesting parameter. Column 3 reports the total (bolometric) luminosity of this besting fitting black body and Column 4 shows the ratio of this bolometric luminosity to the 2–10 keV X-ray luminosity (from Table 3).

source name	blackbody T (keV)	blackbody L_B (10^{43} erg s $^{-1}$)	L_B/L_{2-10}
Mrk 335	$0.14^{+0.02}_{-0.01}$	1.3	0.47
NGC 3516	0.08 ± 0.01	1.2	0.45
NGC 4051	0.12 ± 0.01	0.023	0.80
NGC 5548	$0.24^{+0.03}_{-0.02}$	0.13	0.024
Mrk 841	$0.11^{+0.07}_{-0.04}$	1.3	0.22

show superluminal motion of knots within the radio jet; Cohen et al. 1977).

4.4 Soft excesses

Soft excesses are clearly seen in the data for Mrk 335, NGC 4051 and Mrk 841, as mentioned above. A thorough investigation of soft excesses in the current sample is hampered by the following issue: soft excesses are expected to be most noticeable below ~ 0.6 keV. However, this is the energy below which SIS calibration uncertainties exist. In principle, the most powerful technique for examining soft excesses would be simultaneous fitting of *ROSAT* PSPC and SIS data. Unfortunately, such joint spectral fitting suffers from the problems of non-simultaneous observations and cross calibration problems.

For these reasons a detailed study of soft excesses was not performed. However, for completeness, a black-body component (subject to neutral and ionized absorption) was added to model-B and the data were refitted. To avoid being biased by calibration uncertainties below 0.6 keV, all data below this energy were discarded. Each source fell into one of three categories:

(A) *No significant soft excess (17 objects)* : For most sources the addition of the extra black body component led to no significant statistical improvement in the quality of the fit (according to the F-test using a 99 per cent confidence threshold; Bevington 1969). Such a harsh significance level was set to protect against any small calibration uncertainties affecting this result. Furthermore, the addition of the black-body component did not affect the best-fitting values of the other model-B parameters. Sources in this category are Fairall 9, Mrk 1040, 3C 120, NGC 2992, 3C 273, NGC 4593, MCG–6–30–15, IC 4329a, Mrk 290, 3C 382, 3C 390.3, ESO 141-G55, NGC 6814, Mrk 509, MR 2251–178, NGC 7469 and Mrk 926.

(B) *Statistically significant soft excess (5 objects)* : For most of the remaining sources, a small soft excess was inferred by fitting of the black body component. Sources in this category are Mrk 335, NGC 3516, NGC 4051, NGC 5548 and Mrk 841. These soft excesses signal a gentle change in spectral index below 1 keV and do not affect the other fit parameters (in particular Γ , $\tau_{0.7}$ and $\tau_{0.8}$) significantly. Details

of the black-body fits are reported in Table 5. Note that the total luminosity of the black body component from these fits is always less than the 2–10 keV luminosity. This is in agreement with expectations based on reprocessing models for soft excess components.

(C) *A dramatically different model is inferred by inclusion of a black-body component (2 objects)* : For NGC 3227 and NGC 3783, a *qualitatively* different spectral model results from the addition of the black body component. In both cases a strong and very soft excess produces a large change of spectral slope such as to mimic the effect of one of the oxygen edges. Including the slightly less well calibrated soft end of the SIS range (0.4–0.6 keV) strongly argues against these soft excess models: the spectral models strongly diverge (factor of 5–10) from the data over this small energy range by an amount far in excess of any calibration uncertainty. Thus, we reject these soft excess models in favour of pure warm absorber models.

5 ONE-ZONE PHOTOIONIZATION MODELS

Photoionization is believed to dominate the physics of the warm absorbing material. This belief results from the very high and variable ionization state. Quantitative evidence for this comes from the observed anti-correlation between the O VIII absorption edge depth and the primary ionizing flux observed during the long observation of MCG–6–30–15 (Otani et al. 1996). Many authors have addressed the issue of warm absorption by fitting spectral models constructed with a standard photoionization code such as *CLOUDY* (Ferland 1991). Such codes solve the equations of thermal and ionization equilibrium for the situation in which ionizing radiation (with a given incident flux and spectral form) passes through a slab of Thomson-thin matter. Most authors consider only one-zone models in the sense that the absorbing material is taken to be a slab with uniform properties throughout. These models are then characterised by the column density of the ionized plasma, N_w , and the ionization parameter, ξ , defined by

$$\xi := \frac{L}{nR^2} \quad (4)$$

where n is the number density of the warm plasma and R is the distance of the slab of plasma from an ionizing source of radiation with isotropic ionizing luminosity L .

A caution is in order. Spectral variability of MCG–6–30–15 strongly argues for a multi-zone absorber (see Section 6.2.1 and Otani et al. 1996). The simultaneous UV/X-ray studies of NGC 3516 by Kriss et al. (1996a,b) also imply the existence of a complex stratified ionized absorber. Thus, one-zone photoionization models can only be regarded as a useful parameterisation of the spectral data and the physical quantities resulting from spectral fitting of such models cannot be regarded as measurements of true physical quantities. For this reason, I have not phrased the present discussion of ionized absorbers in terms of N_w and ξ . Instead, I have concentrated on the phenomenological two-edge parameterisation of Sections 3 and 4.

For completeness (and to provide a useful comparison with other work), those objects displaying statistically significant O VII and/or O VIII absorption edges were examined using *CLOUDY* models of the type described above. The

Table 6. Results from spectral fitting with a one-zone photoionization model (model-C). Column 2 gives the best fitting photon index. Column 3 gives the best fitting column density of intrinsic neutral absorbing material (placed at the redshift of the source). Columns 4 and 5 give the best-fitting column density and ionization parameter ξ of the warm photoionized plasma. Column 6 reports the goodness of fit parameter. Errors and limits are shown at the 90 per cent confidence level for one interesting parameter ($\Delta\chi^2 = 2.7$).

source name	Photon Index Γ	Intrinsic N_{H} (10^{20} cm^{-2})	N_{W} (10^{20} cm^{-2})	ξ (erg cm s^{-1})	χ^2/dof
NGC 3227	1.49 ± 0.02	< 3	36^{+5}_{-8}	17^{+8}_{-4}	1390/1436
NGC 3516	$1.86^{+0.05}_{-0.02}$	< 1.7	100^{+7}_{-5}	30 ± 1	1251/1035
NGC 3783	1.66 ± 0.01	$4.7^{+1.9}_{-1.6}$	204 ± 5	45^{+3}_{-2}	1503/1371
NGC 4051	$1.89^{+0.04}_{-0.02}$	< 0.7	11^{+7}_{-4}	10^{+10}_{-4}	1538/1336
NGC 4593	$1.93^{+0.05}_{-0.03}$	$1.0^{+1.0}_{-0.8}$	26^{+10}_{-5}	23^{+7}_{-5}	1416/1385
MCG-6 – 30 – 15	1.97 ± 0.01	$0.5^{+0.5}_{-0.4}$	57^{+3}_{-2}	21 ± 1	2865/2394
IC 4329a	1.76 ± 0.02	26 ± 1	25^{+5}_{-2}	9^{+1}_{-3}	2232/1779
NGC 5548	$1.89^{+0.02}_{-0.01}$	< 0.1	51^{+4}_{-5}	35 ± 2	1792/1627
Mrk 290	$1.80^{+0.10}_{-0.07}$	$1.1^{+2.4}_{-1.1}$	89^{+3}_{-2}	45^{+9}_{-10}	958/1011
3C 382	$2.00^{+0.12}_{-0.02}$	$1.3^{+2.2}_{-1.0}$	32^{+12}_{-8}	34^{+6}_{-7}	1612/1446
Mrk 509	$1.90^{+0.06}_{-0.03}$	$1.4^{+1.3}_{-0.7}$	26^{+14}_{-10}	48^{+11}_{-16}	1559/1494
MR 2251-178	$1.70^{+0.05}_{-0.03}$	< 1.3	50^{+20}_{-10}	43^{+12}_{-8}	777/840

model is the same as model-B except that the warm absorber is modeled using the photoionization model rather than the two-edge parameterisation. This is denoted as model-C. In detail, CLOUDY was used to construct a three-parameter grid of models with Γ , N_{W} and ξ taken to be the variables. The absorber was modelled as a geometrically-thin slab at a distance of 10^{16} cm from a point source of radiation with ionizing luminosity $10^{43} \text{ erg s}^{-1}$ (with a power-law spectrum extending from 13.6 eV to 40 keV with photon index Γ). Models are then computed for various values of the absorber electron number density, n , column density, N_{W} , and photon index, Γ . Since the state of such photoionized gas is dominated by absorption of EUV and soft X-ray photons, this simplistic input spectrum will suffice for the current application in which we are interested in gross features of the soft X-ray opacity. The ionization parameter ξ was then computed from equation (4). For a very large range of parameter space, the effects of differing n are completely described by the ionization parameter ξ . The results of these fits are shown in Table 6.

It is interesting to compare the detailed fits of the simple two-edge model (model-B) with those of the one-zone photoionization model (model-C). Several interesting points can arise from such a comparison. First, the assertion that the two-edge model provides a good description of the warm absorber can be tested. Secondly, spectral structure beyond the two-edge model can be addressed. Thirdly, failures of the one-zone models can be probed. Here, the warm absorber fits for two objects (NGC 3783 and MCG-6 – 30 – 15) are examined in detail.

5.1 NGC 3783

A two-edge fit shows NGC 3783 to have the deepest ionized oxygen edges of the current sample. These edges were first found and extensively investigated with the *ROSAT* PSPC (Turner et al. 1993a). Also, George, Turner & Netzer (1995) report the detection of O VII and O VIII recombination lines (at 0.57 keV and 0.65 keV in the source rest frame)

using *ASCA*. Thus, this object provides a good test case with which to probe details of the ionized absorption.

The two-edge parametrization of the warm absorber in NGC 3783 results in systematic residuals. In particular, there is a small excess of counts at $\sim 1 \text{ keV}$ and a broad deficit of counts between 1–2 keV. Given the extreme nature of this ionized absorber (inferred from the oxygen edge fits), these may be due to unmodelled absorption edges of other species and/or emission lines. Figure 6 addresses this issue. Whilst the photoionization model confirms that the dominant effect is indeed modelled by two ionized oxygen edges, it reveals the presence of an additional absorption edge at $\sim 1.2 \text{ keV}$ identified as the K-shell edge of Ne IX. The onset of this extra-edge, and the consequent diminishing of the O VIII edge explains some, but not all, of the residuals seen in the simple two-edge fit.

5.2 MCG-6 – 30 – 15

The extremely long observation of this bright source leads to very good quality data at the energies characteristic of the warm absorber. Complexities beyond the oxygen edge model (model-B) are likely to be detectable in data of this quality. Indeed, this object is (statistically speaking) described the worst by the simple two-edge model. Figures 7a,c shows the best fitting two-edge model (model-B) and the unfolded SIS data for this object. The poor quality of the fit largely results from a mismatch between the model and the data at $\sim 0.7 \text{ keV}$ (just below the energies of the O VII absorption edge threshold). Fitting the data with a one-zone photoionization model (Figs. 7b,d) produces a much better fit ($\Delta\chi^2 = 155$) due to the emergence of a small O VI edge at 0.68 keV. However, as with NGC 3783, the photoionization calculation confirms that the two-edge model is a good approximation to the effects of the ionized absorption. Note that the existence of this O VI edge may falsely imply a small redshift of the O VII edge when a two-edge model is fitted leaving the edge threshold energies as free parameters.

The one-zone photoionization model also has failures:

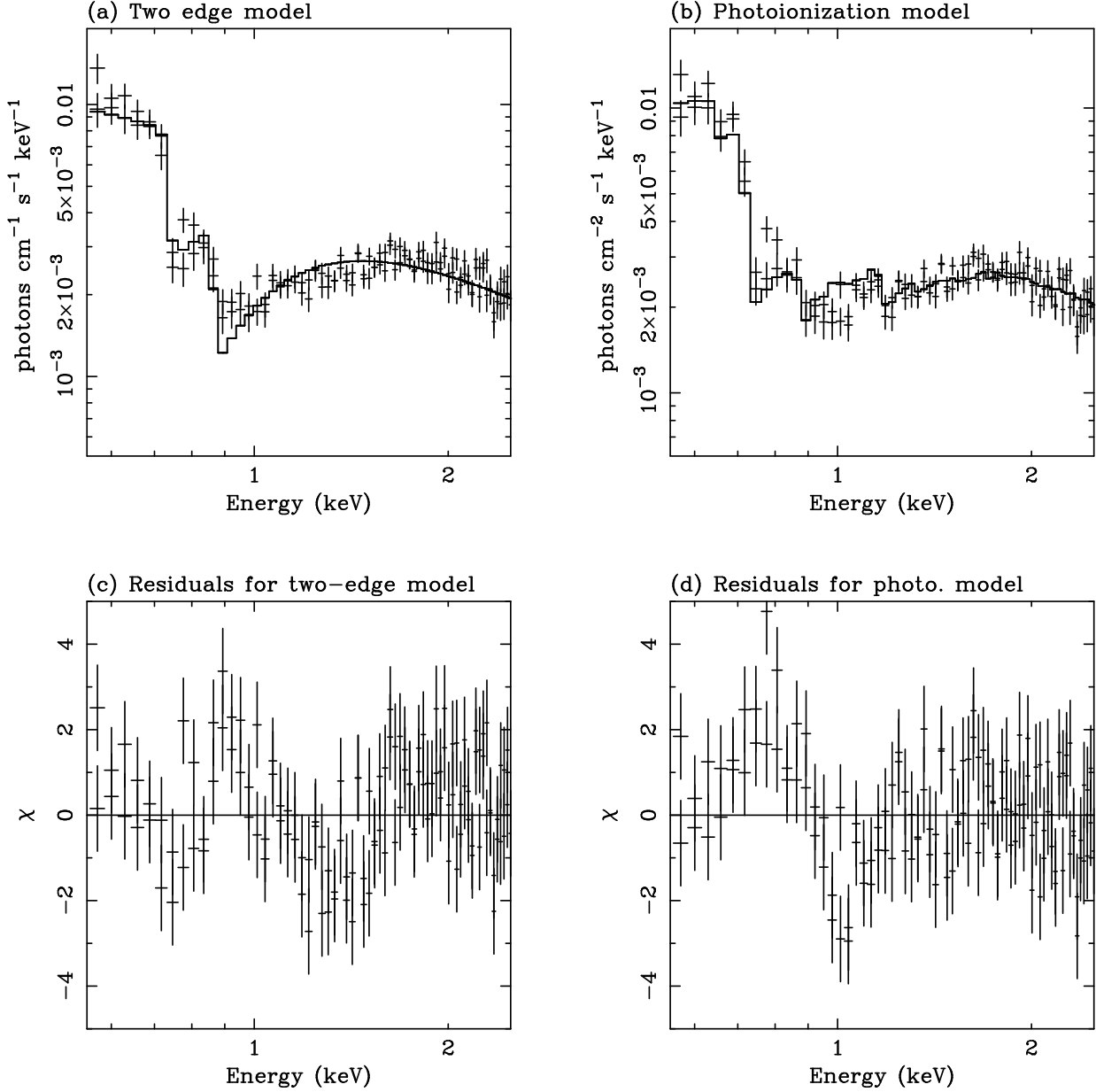


Figure 6. The warm absorber in NGC 3783. Panel (a) shows the best fit two-edge model (model-B) and the unfolded SIS data. Panel (b) shows the best fit photoionization model (model-C) and the unfolded data. Panels (c) and (d) show the deviations of the data from the two-edge and photoionization models, respectively.

it predicts an unobserved Ne IX K-shell edge at ~ 1.2 keV and fails to reproduce an excess of emission at ~ 0.6 keV (most likely recombination line emission from highly ionized oxygen species). This failure is most likely related to the one-zone nature of the model. To see this, note that (for a given ionizing spectrum) the depths of the O VII and O VIII edges uniquely determine the ionization parameter and column density of any one-zone warm absorber model that is fitted to the spectrum. The predicted depths of all other absorption edges are therefore fixed once the spectrum has fitted the oxygen edges. If the absorber is multi-zoned, the state of the absorber is no longer uniquely determined

by the depths of the oxygen edges. Hence, multi-zone absorbers can produce combinations of absorption edges that are not possible from one-zone absorbers.

5.3 Summary of comparison between photoionization model and phenomenological (two-edge model) model

To summarize this Section, it has been explicitly shown that the main observable effects of the warm absorber in the *ASCA* band are K-shell absorption edges of O VII and O VIII at 0.74 keV and 0.87 keV respectively. In addition, K-

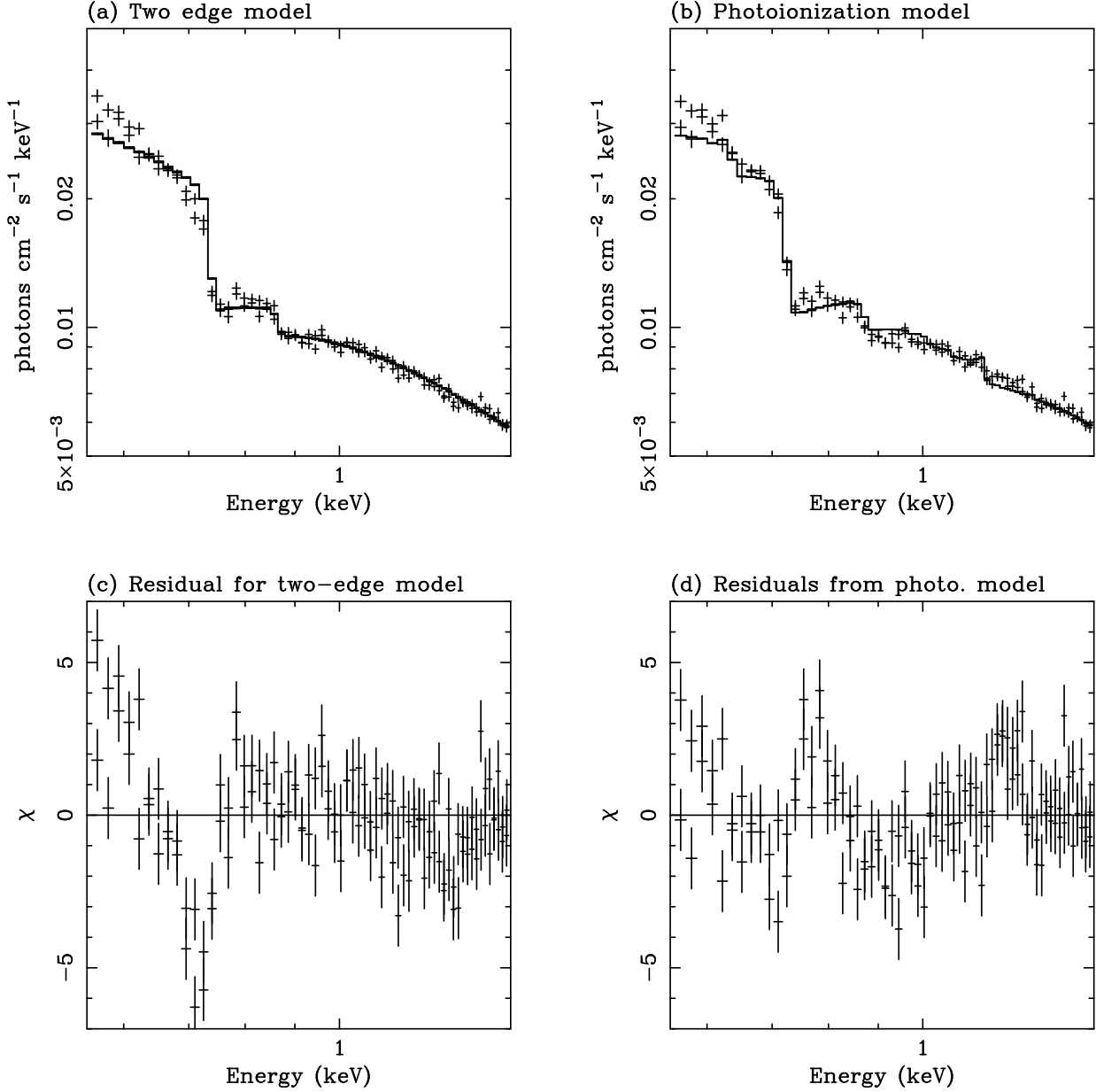


Figure 7. The warm absorber in MCG-6 – 30 – 15. Panel (a) shows the best fitting simple two-edge fit (model-B) and the unfolded SIS spectrum. Panel (b) shows the best fitting photoionization model (model-C) and the unfolded SIS data. Panels (c) and (d) illustrate the deviations from the two-edge and photoionization model, respectively.

shell absorption edges of O VI and Ne IX, at 0.68 keV and 1.2 keV, respectively, can also be observed in high quality *ASCA* data. For comparison to other work, those objects displaying statistically significant oxygen edges have been fitted with a one-zone photoionization model based on the code *CLOUDY* (Ferland 1991). Although these models provide a useful parameterisation of the data, the belief that multi-zone absorption is important means that the physical parameters derived from such models must be treated with caution. For this reason, the current paper concentrates on the phenomenological, two-edge description of the warm absorber.

6 SPECTRAL VARIABILITY

6.1 Motivation

The previous sections have considered the time-averaged spectra of this AGN sample. In this section, the variability properties are briefly examined. A detailed study of the continuum variability properties is presented elsewhere (Nandra et al. 1996a). Here I focus on spectral variability that is relevant to a discussion of the warm absorber.

The response of the photoionized absorber to changes in the primary ionizing continuum provides an important probe of this plasma. In a simple one-zone model, the col-

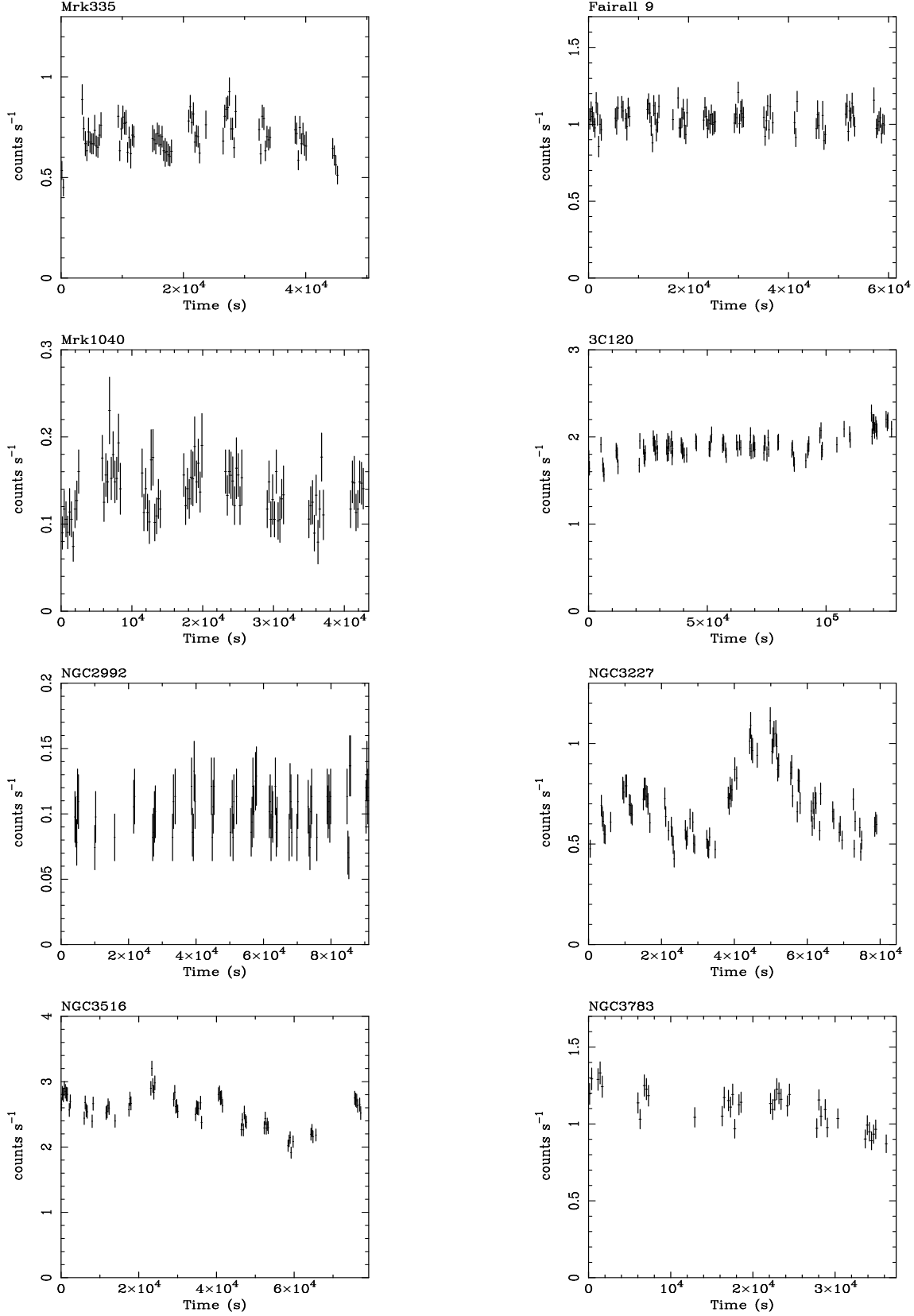


Figure 8.

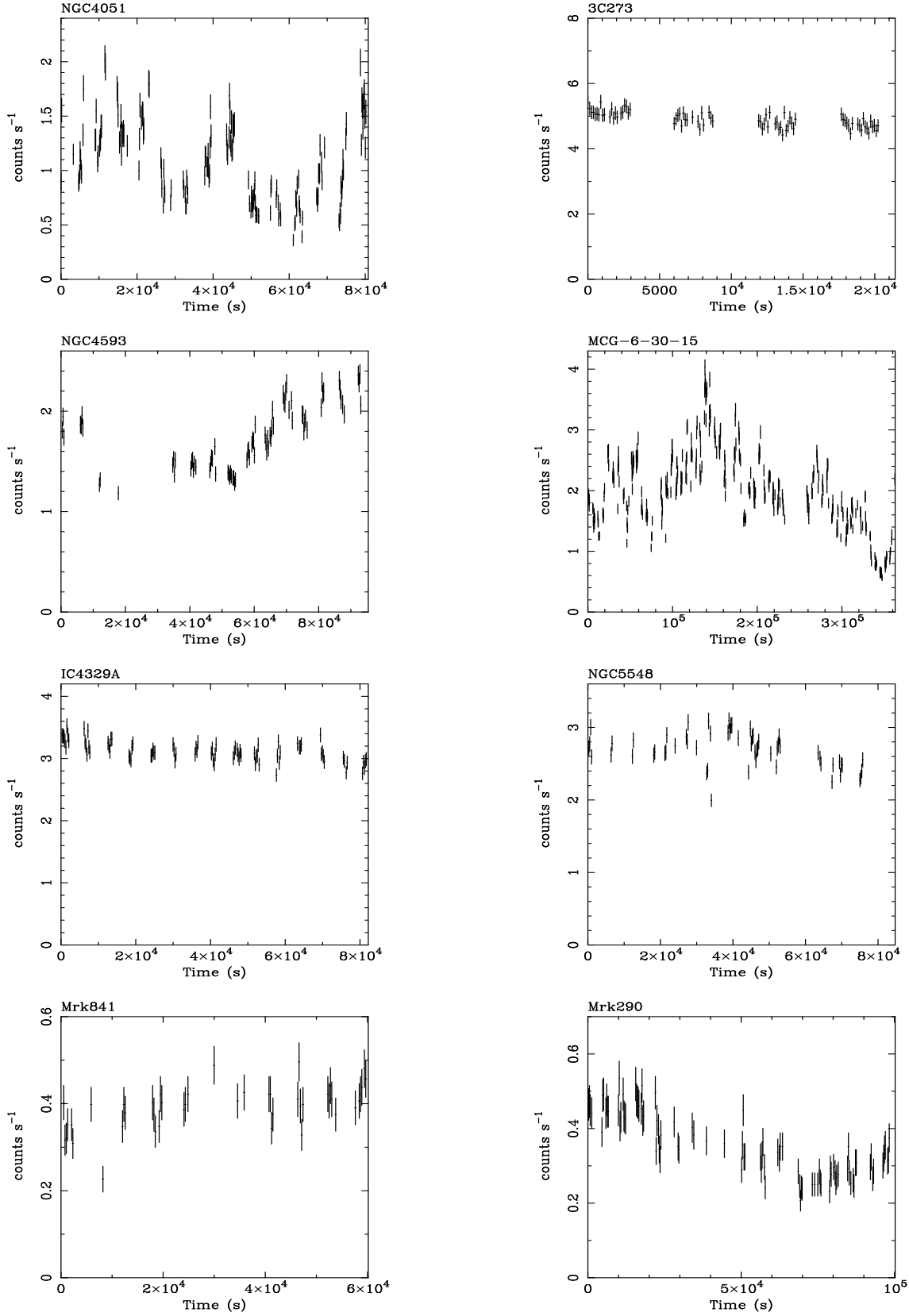


Figure 8. cont.

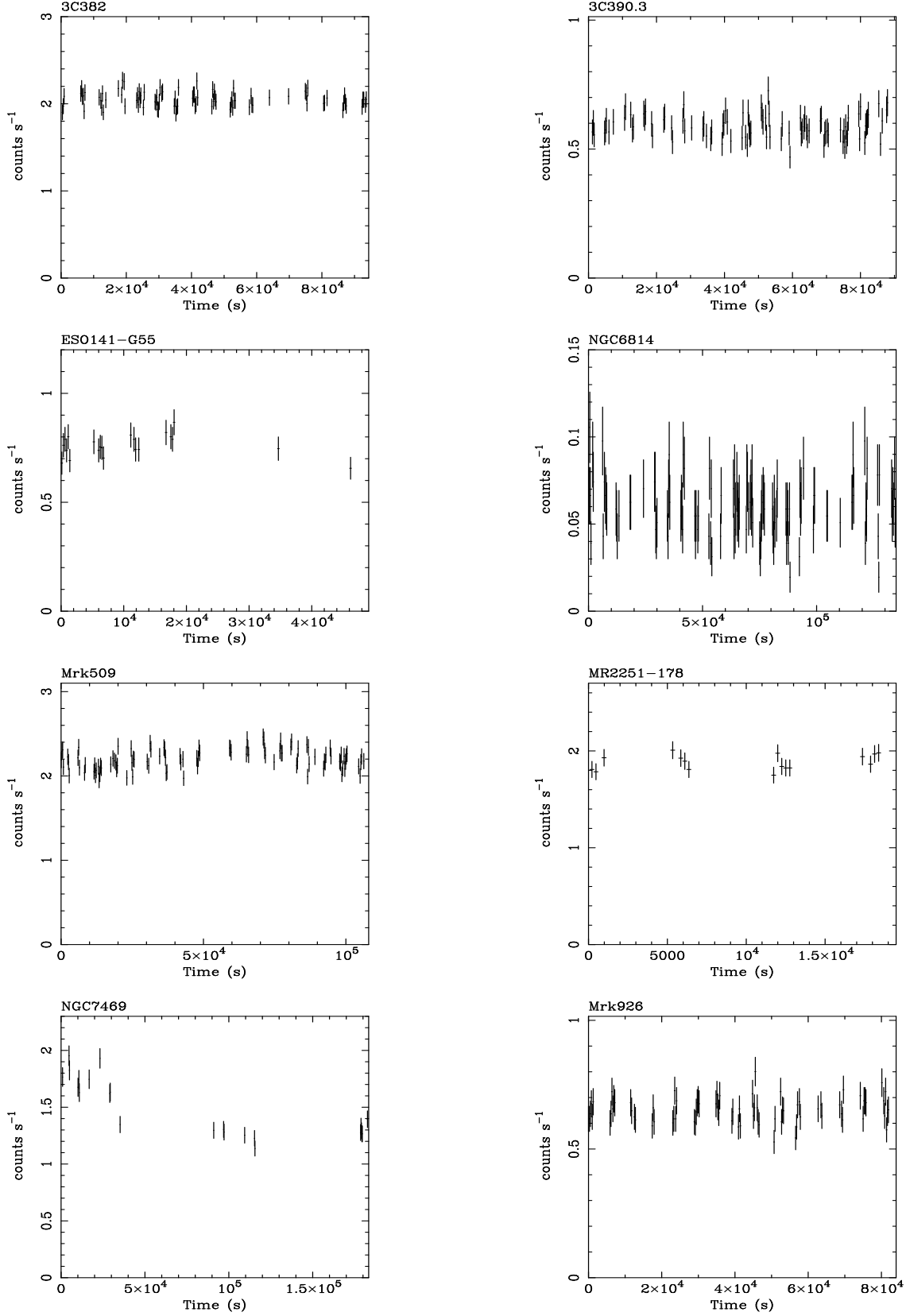


Figure 8. cont. Full-band SIS0 light curves for the 24 objects of this sample. Significant variability is detected in 16 out of 24 objects. See the text for a detailed discussion.

umn density would be expected to remain constant whilst the ionization parameter responds to changes in the continuum flux on the recombination timescale [see Reynolds et al. (1995) for a discussion of the relevant timescales.] In practice, the observed spectral variability in at least some objects tends to disagree with this simple picture. Under these circumstances, the spectral variability is presumably providing information on the structure of the complex absorbing regions.

6.2 Rapid spectral variability

A systematic search for rapid spectral variability (i.e. within the duration of a single observation) was performed using the hardness ratio technique of Reynolds et al. (1995). SIS0 light curves were extracted for each object in the full *ASCA* band (0.4–10 keV) and two restricted energy bands: a soft band at 0.7–1.3 keV (which suffers from the effects of warm absorption) and a hard band at 2.5–5.0 keV (representing unabsorbed continuum). The hardness ratio \mathcal{R} can then be defined as

$$\mathcal{R} = \frac{2.5 - 5 \text{ keV count rate}}{0.7 - 1.3 \text{ keV count rate}} \quad (5)$$

For a fixed primary spectrum, changes in the warm absorber parameters will lead to changes in the value of this hardness ratio.

Figure 8 displays the full band light curves for the sample objects. Many of the objects show clear large amplitude variation during the *ASCA* observation. The null hypothesis of a constant count rate is rejected at 90 per cent confidence (using a standard χ^2 test; Bevington 1969) in all except 8 of the sample sources (Fairall 9, Mrk 1040, NGC 2992, 3C 382, 3C 390.3, ESO 141-G55, MR 2251-178 and Mrk 926). NGC 2992 and Mrk 1040 have small count rates (SIS0 count rate is 0.082 cts s^{-1} and 0.12 cts s^{-1} respectively) compared to all other objects in the sample except NGC 6814. Thus, only dramatic variability would be detectable during the observation of these faint source. The other sources for which primary variability was not detected are all powerful sources with a 2–10 keV luminosity, $L_{2-10} > 10^{44} \text{ erg s}^{-1}$. In fact, only 3 out of 9 sources in the sample with $L_{2-10} > 10^{44} \text{ erg s}^{-1}$ show statistical evidence for variability. In contrast, 14 out of 15 less powerful sources ($L_{2-10} < 10^{44} \text{ erg s}^{-1}$) show statistical evidence for variability. This is in agreement with the well established luminosity-variability time scale relationship of AGN (Green, McHardy & Lehto 1993).

The hardness ratio \mathcal{R} as a function of time along the light curve was constructed in order to search for warm absorber variability. This study is severely hampered by photon statistics and only the brightest and most variable sources might be expected to show unambiguous short term variations of the hardness ratios. Indeed, the null hypothesis of a constant \mathcal{R} could only be rejected with 90 per cent confidence in the case of 2 objects (NGC 3227 and MCG-6 – 30 – 15). I now discuss the variability of these two objects individually.

6.2.1 MCG-6 – 30 – 15

Spectral variability of this object as observed by *ASCA* has been previously reported by Fabian et al. (1994a), Reynolds et al. (1995), Otani et al. (1996) and Iwasawa et al. (1996). Otani et al. (using the same dataset as that analysed here) find that the soft spectral variability is characterised by an O VII edge with a constant depth and an O VIII edge whose depth anticorrelates with the ionizing flux (which varies by a factor of 7 during the observation). They show that this is *incompatible* with any one-zone photoionization model and deduce that a two-zone (or multizone) model is needed.

6.2.2 NGC 3227

Ptak et al. (1994) have performed a detailed analysis of the spectral variability displayed by NGC 3227 during this *ASCA* observation. The data are consistent with behaving in a similar manner to MCG-6 – 30 – 15 (i.e. constant O VII edge and variable O VIII edge). However, it is difficult to reach unambiguous conclusions due to poor photon statistics: in particular, the data cannot rule out a variable primary power-law index modified by a constant warm absorber.

7 NOTES ON INDIVIDUAL OBJECTS

7.1 Radio-Quiet sources

7.1.1 Mrk 335

The Seyfert 1 galaxy Mrk 335 possesses a strong soft excess apparent below 1 keV which is readily observable both in the *ASCA* data presented here and the BBXRT results of Turner et al. (1993b). Turner et al. suggest the presence of ionized absorption on the basis of a joint *Ginga*/BBXRT analysis. The absence of any obvious ionized absorption in the present *ASCA* data suggests either that this absorption is variable or that the supposed warm iron edge seen in the *Ginga* data had some other origin. One possibility is that the sharp drop at $\sim 7\text{--}8 \text{ keV}$ that is characteristic of an iron emission line from a relativistic disk may have been confused with K-shell absorption from highly ionized iron in the *Ginga* data.

7.1.2 Fairall-9

Fairall-9, a luminous Seyfert 1 galaxy, displays a strong and well detected broad fluorescent iron line (with $W_{\text{Fe}} = 380_{-100}^{+150} \text{ eV}$) and a high-energy tail. Figure 9 demonstrates these features which are well fitted by line emission from a relativistic accretion disk (with inclination $27 \pm 5^\circ$) and a strong Compton reflection continuum (Otani 1995). The strength of the iron line can be plausibly explained as due to an enhancement in iron abundance by a modest factor (George & Fabian 1991; Reynolds, Fabian & Inoue 1995). Reverberation effects, most likely associated with time-delayed reflection from the putative molecular torus, have to be invoked to reconcile the observed hard tail with expectations from Compton reflection models.

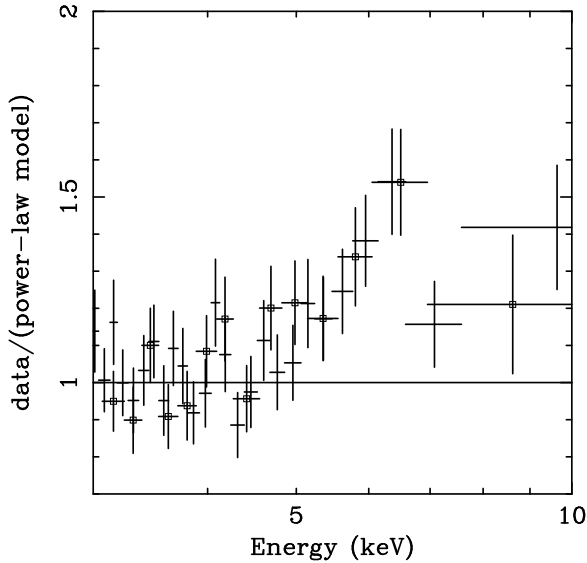


Figure 9. Ratio of the hard-band *ASCA* data for Fairall-9 to the underlying primary continuum model (defined by fitting the data in the 1–4 keV by a simple power-law spectrum). The broad iron line can be seen, as can a hard tail.

7.1.3 Mrk 1040

The *ASCA* observation of Mrk 1040 has been presented previously in Reynolds, Fabian & Inoue (1995). In the present work, we model the soft complexity of this source as a combination of neutral absorption and O VII and O VIII edges in order to force a comparison with the classical warm absorber sources. However, due to the small count rate and high Galactic line-of-sight absorption ($7.07 \times 10^{20} \text{ cm}^{-2}$; Elvis, Lockman & Wilkes 1989), the exact nature of the soft complexity is unclear and several alternative models are explored in Reynolds, Fabian & Inoue (1995). The intrinsic neutral absorption is probably related to the ISM of the host galaxy which possesses a large inclination (Amram et al. 1992).

7.1.4 NGC 2992

The 2–10 keV flux of NGC 2992 has been found to have decreased by a factor of ~ 20 during the past 16 years (Weaver et al. 1996). During that time, its X-ray spectrum has changed from being that of a typical Seyfert 1 galaxy to an extremely hard spectrum. The *ASCA* spectrum is well described by an absorbed power-law with photon index $\Gamma = 1.25$, very much harder than any other source in the present sample, and an narrow (unresolved) neutral iron fluorescence line with equivalent width 560 eV. Weaver et al. (1996) present a detailed study of the *ASCA* spectrum and suggest this spectrum to be dominated by a Compton reflection continuum that remains once the intrinsically steep primary continuum has faded (presumably due to light travel time effects). Significant neutral absorption and a strong soft excess are also required to make this hypothesis consistent with the *ASCA* data. They identify the putative molecular

torus as a natural site for the origin of this time-delayed reflection continuum.

7.1.5 NGC 3227

The rapid spectral variability of this object has been discussed in Section 6.2.2. As with MCG–6–30–15, such variability strongly suggests a multi-zone warm absorber.

7.1.6 NGC 3516

Kriss et al. (1996a) present an analysis of a later *ASCA* observation (1995 March 11/12) of the Seyfert 1 galaxy NGC 3516 than that presented here (2 Apr 1994). It is found that the source has a similar luminosity in both epochs. The inferred oxygen edge depths are also consistent with not having changed between the two epochs. Simultaneous observations with the Hopkins Ultraviolet Telescope (HUT) were also performed (Kriss et al. 1996b). Kriss et al. show that the UV and X-ray data combined strongly argue for a multizone ionized absorber containing a large range of ionization states. They also show how detailed photoionization modelling of the 1995 *ASCA* data hints at a multizone absorber.

7.1.7 NGC 3783

The Seyfert 1 galaxy NGC 3783 is one of the two objects displaying deep, warm oxygen edges but little or no optical/UV reddening (the other being NGC 3516). The photoionized absorber has been discussed in Section 5.1. Alloin et al. (1995) have presented a snapshot of the continuum emission from radio wavelengths through to γ -rays. They show the existence of a classical big blue bump in the UV (confirming the small UV extinction towards this source) and an IR bump. The IR bump is interpreted as originating from dust at temperatures ranging from the sublimation temperature ($T \sim 1500 \text{ K}$) down to relatively cool grains ($T \sim 200 \text{ K}$). These observations support the hypothesis of the existence of dusty warm (photoionized) plasma which, in this object, is out of the line of sight to the central continuum source (see Sections 4.2.2 and 8.2.2).

7.1.8 NGC 4051

The soft X-ray properties of this Seyfert 1 galaxy are complex. The time-averaged soft *ASCA* PV spectrum (Mihara et al. 1994 and the present work) can be explained as a combination of a primary power-law, a black-body soft excess and the effects of ionized absorption. The present work completely agrees with that of Mihara et al. (1994). The black body soft excess has a best fitting temperature $kT = 0.12 \pm 0.01 \text{ keV}$ and a bolometric luminosity $L_B = 2.3 \times 10^{41} \text{ erg s}^{-1}$.

Complex spectral variability has been reported by Guainazzi et al. (1996) during a later *ASCA* observation of NGC 4051. These authors find that in a two-edge parameterisation, both the best fitting edge depth and edge energies increase when the source enters a low state. However, it is unclear how to interpret these results: a complex interplay of a variable ionized absorber with a variable soft

excess could lead to misleading results when an oversimplified spectral model is fitted. An unidentified spectral feature at ~ 0.9 keV may also affect conclusions about spectral variability. Higher spectral resolution observations with future missions (e.g. *ASTRO-E* and *AXAF*) will be invaluable in understanding this complex source.

7.1.9 MCG-6-30-15

This object has been discussed in the introduction and Sections 5.2 and 6.2.1.

7.1.10 IC 4329a

The Seyfert 1 galaxy IC 4329a displays a strong unmodelled high energy excess after fitting with model-B. Cappi et al. (1996) model this hard excess as the onset of a very strong Compton reflection continuum. Time lag effects have to be invoked to obtain such a reflection component. As shown in Cappi et al., the iron line is weak ($W_{\text{Fe}} \approx 90 \pm 30$ eV) once the reflection continuum has been included. If this is the correct spectral model, such a weak line requires an iron underabundance and/or an ionized disk. This is in contrast to many other well studied Seyfert galaxies.

7.1.11 NGC 5548

The oxygen edges of the warm absorber in the famous Seyfert 1 galaxy NGC 5548 were first found by the *ROSAT* PSPC (Nandra et al. 1993). A single edge fit to the *ROSAT* data yields an edge depth of $\tau \sim 0.4$, consistent with the values found here and reported in Table 3. The *ROSAT* data also finds a soft excess component which, when modelled as a black body, has a best fitting temperature of $kT = 60_{-20}^{+13}$ eV. This is rather softer than the values found from the *ASCA* data ($kT = 240_{-20}^{+30}$ eV) and suggests either some spectral variability of the soft excess or a complex soft excess. For example, a blackbody soft excess with a hard tail could reproduce these results due to the different bandpasses of *ROSAT* and *ASCA*.

The *ASCA* data presented here have been previously reported in Fabian et al. (1994b). These authors agree with the results obtained here.

7.1.12 MR 2251-178

MR 2251-178 is the most luminous radio-quiet object of the current sample. It was the first object in which a warm absorber was identified (Halpern 1984; Pan, Stewart & Pounds 1990).

Historical spectral variability over the span of 6 *ASCA* observations (all in AO-1) has been examined by Otani (1995). He finds no significant variation in the parameters of the warm absorber, despite changes by almost a factor of two in the continuum X-ray flux. All spectral variability can be attributed to changes in the continuum photon index which is found to correlate with the flux (i.e. the continuum gets steeper when the flux increases). The warm absorber parameters he derives are entirely consistent with those found here.

7.1.13 NGC 7469

These *ASCA* data on the Seyfert 1 galaxy NGC 7496 have been previously presented in Guainazzi et al. (1994). They found a weak ($W_{\text{Fe}} \approx 120$ eV) narrow neutral iron emission line. The present work (which benefits from recently improved high-energy calibration) also finds a very strong ($W_{\text{Fe}} \sim 1$ keV) and very broad ($\sigma \sim 1.2$ keV) emission feature at these energies, although the narrow line can still be seen in the residuals of the best fitting model-B. The relativistic accretion disk emission line model has difficulties explaining such a spectral feature. A full discussion of this will be presented in a future publication.

7.2 Radio-Loud sources

7.2.1 3C 120

As previously mentioned, the broad-line radio galaxy 3C 120 possesses an extremely broad ($\sigma = 1.5_{-0.4}^{+0.6}$ keV) and strong ($W_{\text{Fe}} = 960_{-270}^{+520}$ eV) spectral feature with a centroid energy $E = 6.43_{-0.24}^{+0.23}$ keV. This is not consistent with being iron fluorescence emission from the immediate vicinity of a Schwarzschild black hole. More investigation is required to determine the origin of such features.

7.2.2 3C 273

The radio-loud quasar 3C 273 is the most luminous object of the current sample by more than an order of magnitude. The addition of a broad Gaussian at energies characteristic of iron $K\alpha$ emission leads to a change in the goodness of fit parameter by $\Delta\chi^2 = 32$ for 3 additional degrees of freedom (with best-fitting parameters reported in Table 4). The F-test shows this to be a significant improvement at more than the 99 per cent level. This is contrary to the result of Yaqoob et al. (1994) who find no significant iron line emission. This discrepancy is understandable given small high-energy calibration issues (associated with the X-ray mirror response) that affected the early response matrices. The analysis presented here should be more reliable at detecting comparatively weak broad features at high energies.

7.2.3 3C 390.3

A detailed analysis of these *ASCA* data on the broad line radio galaxy 3C 390.3 has been reported by Eracleous, Halpern & Livio (1996). These authors focus on the nature of the iron $K\alpha$ emission line. In agreement with the present work, they show it to be resolved and consistent with fluorescent emission from cold iron in the accretion disk of this source.

8 DISCUSSION

Prior to discussing some theoretical implications of this work, the main observational results will be briefly reviewed.

8.1 Summary of observational results

8.1.1 Ionized absorption

Ionized (warm) absorption, characterised by the presence of O VII and O VIII K-shell absorption edges, is a common feature in the soft X-ray spectra of this sample of objects. The inclusion of these absorption edges in the spectral fitting of these objects (as in model-B) leads to a statistically significant improvement in 12 out of the 24 objects. Moreover, 9 of these objects have a maximum optical depth greater than 0.2 (90 per cent confidence level) for one or both of the absorption edges. This is approximately the level at which the ionized absorption is visually apparent in the X-ray spectrum (e.g. see Fig. 1). These results are robust to the presence of a black-body soft excess. They are also robust to any currently recognized SIS low-energy calibration issues.

A striking observational result, and one which has received little attention, is that many objects have ionized edge depths in the range 0.2–1.5. There is no a priori reason for values so comparatively close to unity unless some feedback mechanism related to the optical depth regulates the ionized column density.

The present dataset is sufficiently large to examine general trends. When the sample is split into high and low luminosity subsamples of equal size, the low luminosity objects are found to be more susceptible to ionized absorption than the high luminosity objects. However, the interpretation of this result is not straightforward since all of the radio-loud objects fall into the high luminosity subsample. The data is also consistent with there being *no* luminosity dependence and, instead, a dependence on the radio properties of the objects (with radio-loud AGN having weak ionized absorbers in comparison with radio-quiet AGN).

Optical/UV reddening is also related to the properties of the ionized absorber. At the current level of investigation, the trend is best characterised by dividing the sample into three types: unreddened objects with only small O VII edges, reddened objects with appreciable O VII edges and unreddened objects with very large O VII edges. The formal statistical significance of this relation is shown in Section 4.2.2. The O VIII edge may weakly reflect this trend but with much less significance.

8.1.2 Primary continuum

Model-B seems to adequately describe the X-ray reprocessing phenomena relevant in the *ASCA* band. Therefore, the photon index Γ derived from fitting with this model should represent the slope of the primary non-thermal continuum of the central engine. The distribution of photon indices for the full sample has mean $\langle \Gamma \rangle = 1.81$ and dispersion $\sigma = 0.21$. No significant difference between the photon index distributions of radio-loud and radio-quiet objects is found, although the number of radio-loud objects is too small for this to be addressed fully.

8.1.3 Iron lines

Most objects show spectral complexity at energies characteristic of $K\alpha$ emission lines of iron (6–7 keV). A detailed treatment of this emission in a similar sample of radio-quiet objects is presented in Nandra et al. (1996b).

An interesting point to arise from the current work is a

difference between the high energy complexity in the radio-loud and radio-quiet subsamples. The radio-quiet objects generally display cold iron fluorescent emission lines with profiles that agree well with the hypothesis of originating from a relativistic accretion disk. In contrast, the radio-loud objects generally possess significantly broader emission features which are poorly fit by standard relativistic accretion disk models.

8.2 AGN models and ionized absorption

Modern unified AGN models aim to explain the wide diversity of AGN properties in terms of a few physical principles (see Antonucci 1993 for a recent review). Whilst the radio-loud/radio-quiet dichotomy is clearly a fundamental one, most other observable properties can be explained as an orientation effect.

In the spirit of these unification schemes, I hypothesize that all radio-quiet AGN have optically-thin photoionized plasma in the vicinity of the central engine. The frequency of occurrence of observed ionized absorbers would then suggest this material to cover a fraction of the sky $f_c \sim 0.5$ as seen by the primary X-ray source. As will be demonstrated below, the quantities of photoionized plasma involved are significant as are the mass flow rates of this plasma. Thus, this material represents an important component of the central engine environment. Within such a scheme, any observed luminosity dependence of the warm absorption features would correspond to a luminosity dependence of the column density, ionization state and/or covering fraction of warm material.

8.2.1 Location of the warm absorber

The best studied warm absorber, that in MCG–6–30–15, is strongly believed to be comprised of at least two main zones on the basis of a detailed study of its spectral variability (Otani et al. 1996). Other well studied objects also show evidence for a multizone absorber (NGC 3227: Ptak et al. 1994, NGC 3516: Kriss et al. 1996a,b). Thus, it seems most likely that all objects have, to some extent, a multizone absorber if viewed from the correct orientation. In a complete physical picture, these various absorbing regions will represent different parts of some global flow pattern within the AGN. However, for now I simplify the discussion into that of an ‘inner’ absorber and an ‘outer’ absorber.

8.2.2 The outer absorber

In the case of MCG–6–30–15, the outer absorber is the less ionized one and is responsible for much of the O VII edge. Photoionization models characterise this zone as having a column density $N_W = 4.6 \times 10^{21} \text{ cm}^{-2}$ and ionization parameter $\xi = 17.4 \text{ erg cm s}^{-1}$ (Otani et al. 1996). The constancy of this edge, coupled with recombination timescale arguments, imply that this material is tenuous ($n < 2 \times 10^5 \text{ cm}^{-3}$) and at radii $R > 1 \text{ pc}$. These are radii characteristic of the putative molecular torus, the Seyfert 2 scattering medium and narrow line region (NLR).

This material is a significant component of the AGN

environment. Using a one-zone approximation to model the outer absorber, the mass of this ionized plasma is

$$M = 4\pi R^2 N m_p f_c \quad (6)$$

$$\approx 1000 R_{\text{pc}}^2 N_{22} f_c M_{\odot} \quad (7)$$

where $R = R_{\text{pc}}$ is the radial distance of the absorbing region, $N = 10^{22} N_{22} \text{ cm}^{-2}$ is the column density and f_c is the covering fraction. Evaluating for the parameters relevant to MCG-6-30-15 gives $M \gtrsim 500 f_c M_{\odot}$. If the central engine is accreting at more than a few per cent of the Eddington limit, radiation pressure will dominate the dynamics of this material and drive an outflow (Murray & Chiang 1995; Reynolds & Fabian 1995). Suppose the outflow has a velocity $v = 10^3 v_8 \text{ km s}^{-1}$, number density n and volume filling factor f_v at radius R . Further, suppose the flow occurs over a solid angle Ω . Note that $\Omega/4\pi \gtrsim f_c$ since the outflow itself may be cloudy. The mass flow rate is then given by

$$\dot{M}_{\text{abs}} = \Omega R^2 n m_p v f_v \quad (8)$$

$$= \Omega R N m_p v \quad (9)$$

$$\approx 1 R_{\text{pc}} N_{22} v_8 (\Omega/4\pi) M_{\odot} \text{ yr}^{-1} \quad (10)$$

Evaluating using the parameters of MCG-6-30-15 gives $\dot{M}_{\text{abs}} \gtrsim 0.5 (\Omega/4\pi) v_8 M_{\odot} \text{ yr}^{-1}$. This mass flow rate greatly exceeds the accretion rate within Seyfert galaxies (thought to be $\dot{M}_{\text{acc}} \sim 0.01 M_{\odot} \text{ yr}^{-1}$ assuming an accretion efficiency of $\eta \sim 0.1$).

If the warm absorber is dusty, as suggested in the cases of MCG-6-30-15 and IRAS 13349+2438, the dust must reside in this outer absorber: dust would rapidly sublime if present in the intensely irradiated inner absorber. The observed correspondence between the depth of the O VII edge and the optical reddening in the present sample of objects is further circumstantial evidence for dust coincident with the O VII absorbing region. The observed amount of ionized absorption and optically reddening in radio-quiet AGN would then depend solely on orientation. Some lines-of-sight may have no intervening ionized absorber or dust whereas other lines-of-sight may have a dusty ionized absorber. The two objects displaying deep ionized absorption edges and no optical reddening (NGC 3783 and NGC 3516) may be intrinsically unusual or suggest that there are lines-of-sight with a large column of dust free ionized absorption.

The presence of dust in the outer ionized absorber provides clues as to its origin. It is unlikely to originate by cooling from a hot phase (at the Compton temperature of $T \sim 10^6$ – 10^7 K, say). The hot phase would be completely dust free (any dust would be rapidly sputtered) and dust formation from metals in the warm gas ($T \sim 10^5$ K) would be prevented since the gas temperature very much exceeds the sublimation temperature; dust grains could never assemble at such temperatures. Therefore, the dusty outer absorber is likely to originate via heating of previously cold, dusty material. The classical molecular torus of the standard AGN unification schemes provides an obvious source for such cold dusty material. Thus, the outer absorber may represent a radiatively-driven dusty wind from the torus. The fact that the ionized edge depth is often observed to be within an order of magnitude of unity may also be suggestive of the importance of radiation pressure.

A detailed understanding of such outflows is intimately

linked with a physical understanding of molecular tori, a full discussion of which is beyond the scope of the present paper. However, some general considerations hint at the ingredients of a complete model. The dichotomy between type-1 (broad line) and type-2 (narrow line) AGN suggests the existence of a well defined obscuring torus. The outer ionized absorber may constitute material that forms an ionized skin on the inner edge of this torus and is then driven along radial paths by the action of radiation pressure. The ionized dusty material would possess a conical shell-like structure. The opening angle of the flow in the wall of this conical shell (and thus the solid angle subtended by the flow) would depend on the depth of the ionized torus skin. The observations presented here find that ~ 20 per cent (4 out of 20) radio-quiet type-1 AGN possess significant ionized absorption and significant optical reddening. Taking into account the solid angle in which an observer would see a type-2 object (2π – 3π steradians; Antonucci 1993), the dusty ionized outflow covers ~ 5 – 10 per cent of the total solid angle as seen from the central source. This implies either a thick ionized torus skin (~ 0.1 – 0.3 pc thick in order to subtend this solid angle at the primary source) or that the wind is non-radial.

Ionized material may be caused not to follow a radial path and thus be streamed into the line of sight towards the nucleus via the action of magnetic fields. For example, in the centrifugally driven wind model (Blandford & Payne 1982) matter is driven off the surface of an accretion disk and made to stream along a poloidal magnetic field by the action of centrifugal forces and radiation pressure. Any dust present in the disk material will be carried along in this flow and, beyond the sublimation radius, can survive to form a dusty obscuring ‘torus’ (Konigl & Kartje 1994). Observers at small inclination (i.e. face-on) will be free from any obscuring matter and see bare AGN emission. As the inclination is increased, the line of sight may intercept ionized material (corresponding to the outer warm absorber). For still larger inclinations, dusty ionized material may obscure the central engine. Finally, there would be some critical inclination beyond which a very large column of gas (both ionized and cold) and dust blocks the central engine thereby producing a type-2 source. Konigl & Kartje (1994) suggest that the opening angle of the obscuration-free cone increases with luminosity due to the action of radiation pressure on material streaming along the field lines. Such a mechanism may provide a luminosity dependence to the ionized absorption of the type suggested in Section 4.2.1.

Dusty warm plasma is the most likely the source of strong hot infrared bumps seen in the spectra of many AGN. IRAS 13349+2438, probably the best known individual case of a dust warm absorber to date (Brandt, Fabian & Pounds 1996), has a prominent near IR bump with grain temperatures ranging up to ~ 500 K (Beichman et al. 1986; Barvainis 1987; Wills et al. 1992).

8.2.3 The inner absorber

The inner absorber of MCG-6-30-15 possesses a higher ionization parameter than the outer absorber and is responsible for much of the O VIII edge seen when the source is in a low flux state. A one-zone approximation of this absorber yields parameters $N_{\text{W}} = 1.3 \times 10^{22} \text{ cm}^{-2}$ and $\xi = 74 \text{ erg cm s}^{-1}$. The short recombination timescale of

the warm plasma leads to the rapid spectral variability of this object and implies it to be at distances characteristic of the BLR ($R < 10^{17}$ cm). The rapid spectral variability seen in NGC 3227 (and possibly NGC 4051) suggests that MCG-6-30-15 is not unique and such inner absorbers are common.

The presence of an optically-thin component within BLRs has been suggested by detailed examination of the optical/UV broad line properties. Zheng & O'Brien (1990) examined changes in the line profiles and relative strengths of the Ly α , C IV and Mg II broad lines in the Seyfert 1 galaxy Fairall-9. They argued that some of the Ly α emission and practically all of the C IV emission originates from optically-thin clouds in the inner BLR which are heated by an anisotropic radiation field. Ferland, Korista & Peterson (1990) also investigated an optically-thin inner BLR (the 'very broad line region') and suggested that it might account for the UV continuum of Seyfert galaxies. These authors linked such a component to warm absorption features. More recently, a detailed study of the (rest-frame) UV emission line profiles of the radio-quiet quasar Q0207-398 reveal a highly-ionized and outflowing optical-thin plasma within the BLR (Baldwin et al. 1996). The photoionization models examined by these authors show a clear link between these optically-thin BLR clouds and ionized X-ray absorption.

Using the expressions of Section 8.2.2 and assuming a distance of $R \sim R_{\text{BLR}} \sim 10^{17}$ cm suggests that the mass of the inner absorber is $M \sim 1 f_c M_\odot$ for the parameters of Seyfert galaxies. This is comparable with the total mass of the classical (optically-thick) broad emission line clouds (although this is a very model dependent quantity[†]), suggesting that this material is an important component of the BLR.

If the inner X-ray absorber is truly related to the BLR, an understanding of its origin and physical state is intricately linked to an understanding of the BLR generally. Different BLR models would lead to a dramatically different interpretation for the optically-thin material (see discussion in Reynolds & Fabian 1995). A detailed discussion of such models is beyond the scope of this paper.

9 CONCLUSIONS

The primary aim of this work is to study the X-ray spectral properties of an unbiased sample of type-1 AGN using the unprecedented spectral capability of *ASCA*. The sample contains both radio-quiet objects (18 Seyfert 1 galaxies and 2 RQQ) and radio-loud objects (3 BLRG and 1 RLQ)

[†] A lower limit on the mass of the classical broad line clouds can be set by considering H β emission. For MCG-6-30-15, the luminosity in the broad H β line is $L_{\text{H}\beta} \approx 3 \times 10^{40}$ erg s⁻¹ (Pineda et al. 1980). If the line emitting material has volume V and density $n = 10^9 n_9 \text{ cm}^{-3}$, we can write

$$L_{\text{H}\beta} = V n^2 \alpha_{\text{H}\beta} h \nu_{\text{H}\beta} \quad (11)$$

where $\alpha_{\text{H}\beta}$ is the H β effective recombination coefficient ($\alpha_{\text{H}\beta} = 2.0 \times 10^{-14} \text{ cm}^3 \text{ s}^{-1}$; Osterbrock 1989) and $\nu_{\text{H}\beta}$ is the frequency of H β line emission. Rewriting this in terms of the mass M_{BLR} of emitting material and evaluating for MCG-6-30-15 gives $M_{\text{BLR}} = 0.2 n_9^{-1} M_\odot$

and thus comparisons can be drawn between these two broad classes of source. The main results and conclusions are listed below.

(i) Spectral complexity, defined as deviations from the primary power-law spectrum, is common within this sample. In particular, at least 12 out of 24 sources display absorption features due to photoionized material (the so-called warm absorber) implying that the covering fraction of the warm material is $f_c \sim 0.5$. In addition, almost all sources show an excess at energies characteristic of iron K α emission.

(ii) The effect of the warm absorber in the *ASCA* band is well described by two K-shell absorption edges due to O VII and O VIII at 0.74 keV and 0.87 keV respectively. Fully consistent one-zone photoionization models show O VI and Ne IX K-shell edges to be also observable, although the oversimplified assumptions within these models (especially the assumption of a one-zone absorber) leads to certain failures and limits the use of such models. Thus, I focus on the phenomenological two-edge model of the warm absorber. Unmodelled spectral features could lead to false (unphysical) shifts of the edge threshold energies if these energies were left as free parameters. For example, an unmodelled O VI edge (at 0.68 keV) could produce a small redshift of the O VII edge. To avoid this, the edge energies have been fixed at the physical values.

(iii) There is a trend for there to be less ionized absorption (i.e. edge depths are smaller) in either more luminous objects and/or radio-loud objects. The present data cannot distinguish these two possibilities because the radio-loud objects are all amongst the most luminous sources in the sample. It must be noted that there *are* at least two luminous radio-loud objects known, 3C 212 (Mathur 1994) and 3C 351 (Mathur et al. 1994), which display warm absorbers. The existence of this apparent exceptions highlights the need for further study with larger samples.

(iv) Sources displaying significant optical reddening ($X > 1$) also display deep O VII edges. Coupled with other studies of particular objects (MCG-6-30-15 and IRAS 13349+2438), this supports the hypothesis that there is warm photoionized plasma containing dust in thermal equilibrium with the primary radiation field. Within the context of unified AGN models, a radiatively driven wind originating from the molecular torus is a plausible identification of such this material. The large covering fraction of this outflow (as inferred from the frequency of occurrence in this sample) implies that either the torus has a thick ionized skin or some mechanism (e.g. magnetic field) forces a non-radial flow.

(v) Optically thin clouds/filaments within the BLR are also likely to be the source of some warm absorption features. The presence of such material has been suggested by recent detailed optical/UV emission line studies as well as X-ray spectral variability. This material is likely to be an important component of the BLR.

(vi) The iron K α emission is thought to be due to fluorescence within optically-thick cold material irradiated by the primary X-ray continuum. 16 out of 20 radio-quiet objects show resolved broad lines which are consistent with originating from the inner parts of an accretion disk. The corresponding spectral feature in radio-loud objects is found to be significantly broader and poorly fit by standard relativistic disk models. An interesting possibility is that the

presence of a relativistic jet is affecting the nature of this emission.

(vii) Once all reprocessing mechanisms have been modelled, the primary continuum can be studied. The photon index distribution has mean $\langle \Gamma \rangle = 1.81$ and standard deviation $\sigma_\Gamma = 0.21$. There is no significant difference between radio-quiet and radio-loud objects (although the number of radio-loud objects is small).

ACKNOWLEDGEMENTS

I thank Andy Fabian and Kazushi Iwasawa for many useful discussions throughout the course of this work. The referee is thanked for a careful reading of the original manuscript. This research has made use of the NASA/IPAC Extragalactic Database (NED) which is operated by the Jet Propulsion Laboratory, California Institute of Technology, under contract with the National Aeronautics and Space Administration. This work has also made extensive use of data obtained through the High Energy Astrophysics Science Archive Research Center (HEASARC) Online Service, provided by the NASA-Goddard Space Flight Center. I acknowledge the Particle Physics and Astronomy Research Council (PPARC) for support.

REFERENCES

- Alloin D. et al., 1995, *A&A*, 293, 293
 Amram P., Marcelin M., Bonnarel F., Boulesteix J., Afanasiev V., Dodonov S., 1992, *A&A*, 263, 69
 Antonucci R., 1993, *ARAA*, 31, 473
 Awaki H., Koyama K., Inoue H., Halpern J. P., 1991, *PASJ*, 43, 195
 Baldwin J. A. et al., 1996, *ApJ*, 461, 664
 Barvainis R., 1987, *ApJ*, 320, 537
 Bevington P. R., 1969, *Data Reduction and Error Analysis for the Physical Sciences*. McGraw-Hill, New York
 Beichman C. A., Soifer B. T., Helou G., Chester T. J., Neugebauer G., Gillett F. C., Low F. L., 1986, *ApJ*, 308, L1
 Blandford R. D., Payne D. G., 1982, *MNRAS*, 199, 883
 Brandt W. N., Fabian A. C., Pounds K. A., 1996, *MNRAS*, 278, 326
 Burstein D., Heiles C., 1978, *ApJ*, 225, 40
 Cappi M., Mihara T., Matsuoka M., Hayashida K., Weaver K. A., Otani C., 1996, *ApJ*, 458, 149
 Cohen M. H. et al., 1977, *Nat*, 268, 405
 Courvoisier T. J. -L., Paltani S., 1992, *IUE – ULDA Access Guide* no. 4
 Elvis M., Lockman F. J., Wilkes B. J., 1989, *AJ*, 97, 777
 Eracleous M., Halpern J. P., Livio M., 1996, *ApJ*, 459, 89
 Fabian A. C. et al. 1994a, *PASJ*, 46, L59
 Fabian A. C., Nandra K., Brandt W. N., Hayashida K., Makino F., Yamauchi M., 1994b, in Makino F., Ohashi T., eds, *New Horizon of X-ray Astronomy*, Universal Academy Press, Tokyo, p573
 Fabian A. C. et al. 1995, *MNRAS*, 277, L11
 Ferland G.L., 1991, Ohio State University, Astronomy Department Internal Report 91-01
 Ferland G. L., Korista K. T., Peterson B. M., 1990, *ApJ*, 363, L21
 Fiore F., Elvis M., Mathur S., Wilkes B.J., McDowell J.C., 1993, *ApJ*, 415, 129
 George I. M., Fabian A. C., 1991, *MNRAS*, 249, 352
 George I. M., Turner T. J., Netzer H., 1995, *ApJ*, 438, L67
 Green A. R., McHardy I. M., Lehto H. J., 1993, *MNRAS*, 265, 664
 Guainazzi M., Matsuoka M., Piro L., Mihara T., Yamauchi M., 1994, *ApJ*, 436, L35
 Guainazzi M., Mihara T., Otani C., Matsuoka M., 1996, preprint
 Guilbert P. W., Rees M. J., 1988, *MNRAS*, 233, 475
 Halpern J.P., 1984, *ApJ*, 281, 90
 Iwasawa K. et al., 1996, *MNRAS*, in press
 Konigl A., Kartje J. F., 1994, *ApJ*, 434, 446
 Kriss G. A. et al. 1996a, *ApJ*, 467, 629
 Kriss G. A. et al. 1996b, *ApJ*, 467, 622
 Krolik J.H., Kallman G.A., 1987, *ApJ*, 320, L5
 Kwan J. Y., Krolik J. H., 1981, *ApJ*, 250, 478
 Lightman A. P., White T. R., 1988, *ApJ*, 335, 57
 Murray N., Chiang J., 1995, *ApJ*, 454, L105
 Mathur S., 1994, *ApJ*, 431, L75
 Mathur S., Wilkes B., Elvis M., Fiore F., 1994, *ApJ*, 434, 493
 Mathur S., Elvis M., Wilkes B., 1995, *ApJ*, 452, 230
 Matsuoka M., Piro L., Yamauchi M., Murakami T., 1990, *ApJ*, 361, 440
 Matt G., Perola G. C., Piro L., 1991, *A&A*, 245, 63
 Mihara T., Matsuoka M., Mushotzky R. F., Kunieda H., Otani C., Miyamoto S., Yamauchi M., 1994, *PASJ*, 46, L137
 Mushotzky R. F., Fabian A. C., Iwasawa K., Kunieda H., Matsuoka M., Nandra K., Tanaka Y., 1995, *MNRAS*, 272, L9
 Nandra K., George I. M., Mushotzky R. F., Turner T. J., Yaqoob T., 1996a, *ApJ*, submitted
 Nandra K., George I. M., Mushotzky R. F., Turner T. J., Yaqoob T., 1996b, *ApJ*, in press
 Nandra K., Pounds K.A., 1992, *Nat*, 359, 215
 Nandra K., Pounds K. A., 1994, *MNRAS*, 268, 405 (NP94)
 Nandra K., Pounds K. A., Stewart G. C., 1990, *MNRAS*, 242, 660
 Nandra K., Pounds K. A., Stewart G. C., Fabian A. C., Rees M. J., 1989, *MNRAS*, 236, 39P
 Nandra K., Pounds K. A., Stewart G. C., George I. M., Hayashida K., 1991, *MNRAS*, 248, 760
 Nandra K. et al., 1993, *MNRAS*, 260, 504
 Netzer H., 1993, *ApJ*, 411, 594
 Osterbrock D. E., 1989, *Astrophysics of Gaseous Nebulae and Active Galactic Nuclei*, Univ. Science Books, Mill Valley
 Otani C., 1995, PhD thesis, Nagoya Univ.
 Otani C. et al., 1996, *PASJ*, 48, 211
 Pan H.-C., Stewart G.C., Pounds K.A., 1990, *MNRAS*, 242, 177
 Pineda F. J., Delvaile J. P., Grindlay J. E., Schnopper H. W., 1980, 237, 414
 Ptak A., Yaqoob T., Serlemitsos P. J., Mushotzky R. F., Otani C., 1994, *ApJ*, 436, L31
 Reynolds C. S., Fabian A. C., 1995, *MNRAS*, 273, 1167
 Reynolds C. S., Fabian A. C., Inoue H., 1995, *MNRAS*, 276, 1311
 Reynolds C. S., Fabian A. C., Nandra K., Inoue H., Kunieda H., Iwasawa K., 1995, *MNRAS*, 277, 901
 Stark A. A., Gammie C. F., Wilson R. W., Bally J., Linke R. A., Heiles C., Hurwitz M., 1992, *ApJS*, 79, 77
 Tanaka Y., Inoue H., Holt S. S., 1994, *PASJ*, 46, L37
 Tanaka Y. et al., 1995, *Nat*, 375, 659
 Turner T. J., Pounds K. A., 1989, *MNRAS*, 240, 833
 Turner T. J., Nandra K., George I. M., Fabian A. C., Pounds K. A., 1993a, *ApJ*, 419, 127
 Turner T. J. et al., 1993b, *ApJ*, 407, 556
 Veron-Cetty M. P., Veron P., 1993, *ESO Scientific Report* 13
 Ward M. J., Elvis M., Fabbiano G., Carleton N. P., Willner S. P., Lawrence A., 1987, *ApJ*, 315, 74
 Weaver K. A., Nousek J., Yaqoob T., Mushotzky R. F., Makino F., Otani C., 1996, *ApJ*, 458, 160
 Wills B. J., Wills D., Evans N. J., Natta A., Thompson K. L., Breger M., Sitko M. L., 1992, *ApJ*, 400, 96
 Yaqoob T. et al., 1994, *PASJ*, 46, L49
 Zheng W., O'Brien P. T., 1990, *ApJ*, 356, 463